TÉCNICO LISBOA

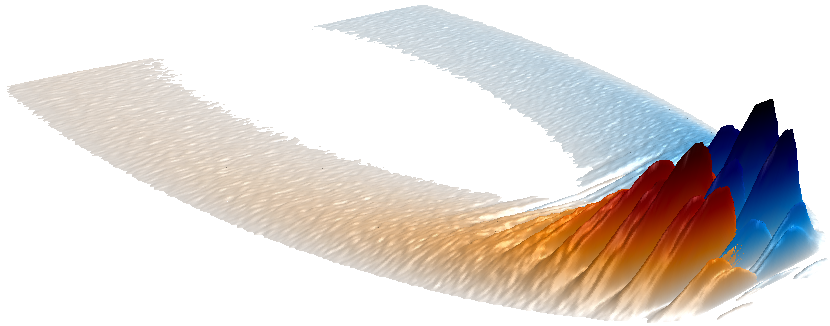

Phase Control of Nonlinear Breit-Wheeler Pair Creation

Bernardo Maria Pereira da Costa de Pessanha Barbosa

Thesis to obtain the Master of Science Degree in

Engineering Physics

Supervisors: Prof. Marija Vranic
Dr. John Palastro

Examination Committee

Chairperson: Prof. Luís Paulo Da Mota Capitão Lemos Alves
Supervisor: Prof. Marija Vranic
Members of the Committee: Prof. Hugo Fernando Santos Terças
Dr. Bertrand Martinez
Prof. Jorge Miguel Ramos Domingues Ferreira Vieira

December 2022

Dedicated to Fernando Barbosa, who would have attempted to read this thesis for sure,
despite not knowing any physics.

Acknowledgements

The present work would be impossible to make without the help of my supervisors Marija Vranić and John Palastro, who I must thank not only for their amazing guidance and support throughout this year but also for showing how physics research is fascinating. This work was crucial for allowing me to see that I will keep doing investigation even after the Master's is over. I would like to thank Bertrand Martinez, Kathleen Weichman, and Dillon Ramsey for a lot of discussions useful for achieving the results present in this work. Also, I want to thank all the team at GoLP for making me feel at home while doing research with them.

Finally, I want to thank the amazing friends I made during these five years at MEFT, without whom my academic life would have been surely less successful and enjoyable, and to who I owe a lot. In specific, I leave a huge thank you to: Filipa, Santos, and Zeca for all the long mornings, afternoons and nights we spent doing experimental physics reports, but always with great attitude and spirit; Comboio, Miguel, and Rita for many Discord calls and support that helped me maintain my sanity during and after the COVID outbreak; Angelo and Niclas for making my Erasmus experience one of the most cherished memories of my life; and Diana for a lot of support in these final months of the Master's, not allowing me to succumb to stress, and bringing a lot of passion back to my life. Muito obrigado a todos! Seria impossível sem vocês.

The work for this thesis has been funded by the project PTDC/FIS-PLA/3800/2021 and the computer simulations have been performed in: the Accelerates cluster, at IST; the MareNostrum cluster, based in the Barcelona Supercomputing Centre in Barcelona, Spain; and LUMI located in CSC's data center in Kajaani, Finland.

Resumo

Plasmas eletrão-positrão existem na vizinhança de objetos astrofísicos, como estrelas de neutrões. Este é um dos motivos que contribui para o interesse geral em estudar os comportamentos destes plasmas, que contrastam fortemente com plasmas de laboratório convencionais ião-eletrão devido à simetria das massas entres as espécies positivas e negativas. A produção de pares eletrão-positrão em quantidade suficiente para observar efeitos coletivos é um desafio em física moderna. Uma maneira de gerar estes pares consiste em colidir um impulso de laser de alta intensidade com um feixe de eletrões relativista. Este esquema permite a produção de fotões de alta energia através da dispersão de Compton não linear, que posteriormente decaem num par eletrão-positrão através da criação de pares de Breit-Wheeler não linear. Uma desvantagem destas experiências atualmente reside no número baixo de positrões produzidos e na interferência com outros processos (como pares produzidos por fotões de bremsstrahlung). Nesta tese, um esquema usando um impulso de laser com duas cores é usado para alcançar a separação espacial dos pares produzidos na interação, e dos eletrões do feixe inicial. Um modelo teórico é introduzido para prever quando ocorre separação de momento das cargas em função dos parâmetros do impulso de duas cores (especialmente, da fase) e simulações Partícula-na-Célula mostram que este efeito dá origem a observáveis mensuráveis em experiências futuras. Simulações com largura de feixe finito mostram a separação física dos pares e a corrente produzida pelo movimento destas, que pode ser controlado variando a fase relativa entre as duas componentes do laser.

Palavras-chave: Física de Plasmas; Criação de pares; Eletrodinâmica Quântica; Códigos Partícula-na-Célula; Lasers de Alta Intensidade; Impulsos de Duas Cores

Abstract

Electron-positron plasmas are present in the vicinity of astrophysical objects, e.g. neutron stars. This is one of the reasons that contribute to general interest to investigate the behavior of these plasmas, which highly contrast regular laboratory ion-electron plasmas due to the symmetry of the species' mass. The laboratory production of electron-positron plasmas in enough amount to observe collective phenomena is a challenge in modern physics. One way to generate electron-positron pairs is to collide an intense laser pulse with a relativistic electron beam. This setup allows for the production of high-energy photons via nonlinear Compton scattering, which afterward decay into electron-positron pairs via nonlinear Breit-Wheeler pair creation. A setback in these experiments currently is that the number of generated positrons is very low, and background signals can interfere with the data collection (e.g. from bremsstrahlung photons decaying into pairs). In this work, a scheme utilizing a two-colored laser pulse is presented to achieve spatial separation of the produced pairs during the laser-beam interaction, and separate them from the original electron beam. A theoretical model is introduced to predict when charge momentum separation occurs in a plane wave as a function of the parameters of the two-colored pulse (most importantly, the laser phase) and Particle-in-Cell simulations demonstrate the effect leads to measurable observables for future experiments. Simulations with a finite spot size laser show the physical separation of the charges and the current produced by their motion, which can be controlled by varying the relative phase of the two laser modes.

Keywords: Plasma Physics; Pair Creation; Quantum Electrodynamics; Particle-in-Cell Codes; High-Intensity Lasers; Two-Colored Pulses

Table of Contents

List of Tables

List of Figures

List of Symbols

Physical Constants

α	Fine structure constant.
$\hbar = \frac{h}{2\pi}$	Reduced Planck's constant.
μ_0	Permeability of free space.
ε_0	Permittivity of free space.
c	Speed of light in vacuum.
h	Planck's constant.

Relativistic Physics

$\gamma = \frac{1}{\sqrt{1-\beta^2}}$	Lorentz factor.
$\vec{\beta} = \frac{\vec{v}}{c}$	β factor.
$F^\mu = \left(\frac{\gamma}{c}\vec{F}\cdot\vec{v}, \gamma\vec{F}\right)$	Four-force.
$F_{\mu\nu}$	Electromagnetic tensor.
$k^\mu = \left(\frac{\omega}{c}, \vec{k}\right)$	Four-wavevector.
$p^\mu = mu^\mu$	Four-momentum.
$u^\mu = (\gamma c, \gamma\vec{v})$	Four-velocity.
$x^\mu = (ct, \vec{r})$	Four-position.

Subscripts

x, y, z	Components of a vector in cartesian coordinates.

List of Abbreviations

PIC Particle-in-Cell.

QED Quantum Electrodynamics.

Chapter 1

Introduction

1.1 Overview

With the recent developments in high-intensity laser facilities, it is possible to reach regimes where Quantum Electrodynamics (QED) effects become relevant in the interaction of a laser with a relativistic electron beam. These facilities, which can reach multi PW powers, are able to deliver intensities on the order of $10^{23} - 10^{24}$ W/cm^2 [1–3]. Plasmas composed of electrons and positrons created by QED processes are theorized to occur in the vicinity of very massive and compact objects, such as neutron stars. [4, 5] This turns our attention to trying to replicate at least some of the physics of these plasmas in a laboratory setup, using intense electric fields to replicate the regime where QED processes allow for the creation of a large number of positrons. Some of the schemes proposed for production of these plasmas include production in electron-laser scattering experiments [6, 7], where the high intensity electromagnetic field is provided by a focused laser, and which I focus on during this study; and the Bethe-Heitler process [8, 9], which is similar to electron-laser scattering, but uses the electric field of a nucleus of an atom with high atomic number. Trapping and accumulating positrons emitted from β^+ decay [10] is also a possibility, but with an added concern due to the annihilation of the positrons with electrons from normal matter. The predominant QED processes when using electron-laser scattering are: radiation reaction, which, given the very high accelerations felt by electrons and positrons in the oscillatory laser fields, results in a significant decrease of particle energy due to the radiated electromagnetic energy; nonlinear Compton scattering [11], where an electron or positron emits a high energy photon in the presence of an intense laser field, losing some of its own energy in the process; and nonlinear Breit-Wheeler pair creation [12], where an energetic photon, also in the presence of the strong laser fields, decays into an electron-positron pair. The sequential and repeated occurrence of these processes can result in a QED cascade. One of the current experimental goals in strong-field plasma QED is to cascade a sufficient number of particles to produce a pair plasma where collective phenomena are observable. Using an electron-laser collision for pair production has the setbacks that the peak intensity of a high intensity laser pulse is quite difficult to determine with precision [13], and that detecting the produced pairs is also a challenge, since the initial beam has electrons which can mix

with the signal, which should (and sometimes can) be avoided [14]. There may also be some other QED processes producing leptons which turn the distinction of pairs produced via nonlinear Breit-Wheeler process more difficult, like pairs produced via Bethe-Heitler process occurring in the background, or by the direct trident process, where an electron immediately releases an electron-positron pair. [15]

In this thesis, I introduce a new scheme using a two-colored laser pulse for generating a bulk electric current during pair creation, which provides a macroscopic signature without the need for a high-density plasma. An analogous setup has been used to show that this current exists in the case of a two-colored laser ionizing atoms [16]. The reason why this system shows this behavior is because the probability of ionizing an atom grows as the intensity of the electric field grows, which favors particle birth in some phases of the pulse. For the pair creation case, the system also has a higher probability of generating pairs if the electric field is stronger, therefore, a net current should be possible to observe, similarly to the ionization case. However, unlike the ionization case, in a pair plasma, both species have the same mass, therefore, a drift can easily be imparted to both electrons and positrons in opposite directions. This separation of charges would allow us to see a macroscopic signature of pair plasma-laser interaction, without needing to generate a high-density plasma, as in other studies of pair plasma group behavior [17]. It may also allow for easier detection of the pairs, since species propagate dominantly in opposite transverse directions.

Here I propose a scheme that utilizes a laser pulse and its second harmonic with an offset in phase, to obtain phase control over the direction of the emitted pairs. In Chapter 2 of this thesis, a theoretical approach is deduced to predict when charge separation occurs in pairs born via nonlinear Breit-Wheeler process in a two-colored laser pulse. In section 2.1 I show that particles born in the middle of the pulse acquire a transverse drift depending on the sign of their charge and in section 2.2 it is shown that the net separation of the charges is dependent on the phase difference between the pulses, just like the case for ionization in electron-ion plasmas [16], not only obtaining a macroscopic effect of the dynamics of an electron-positron plasma without the need to generate a dense plasma, but also creating an electron and positron beam with opposite asymptotic angles. The setup used to demonstrate this effect is sketched in figure 1.1. A relativistic electron beam (in blue) is sent to collide head-on against a laser pulse with two frequencies (represented by the red ellipsoid with another blue one inside it, however, this happens only for representation purposes, and not actually to represent that one pulse has a larger spot size than the other). In gray is represented the path the gaussian laser pulses follow as time evolves. First, when the electrons reach the vicinity of the laser pulse, some hard photons are emitted toward the center of the pulse due to nonlinear Compton scattering. Then, these photons decay into pairs according to the nonlinear Breit-Wheeler pair creation. The pairs then proceed to either drift in opposite directions or not according to the phase offset between the two laser waves.

The predictions made in Chapter 2 are supported by Particle-in-Cell (PIC) simulations run in the framework of OSIRIS [18] with an added Monte Carlo module for the QED processes [19, 20] shown in Chapter 3. Section 3.1 benchmarks the analytical predictions with plane wave simulation against a photon bunch, and in section 3.2 a finite laser both in size and duration collides against an electron beam in order to observe

the effect of phase control in the movement of the leptons, and the overall charge separation and symmetric transverse motion of the electrons and positrons after the interaction.

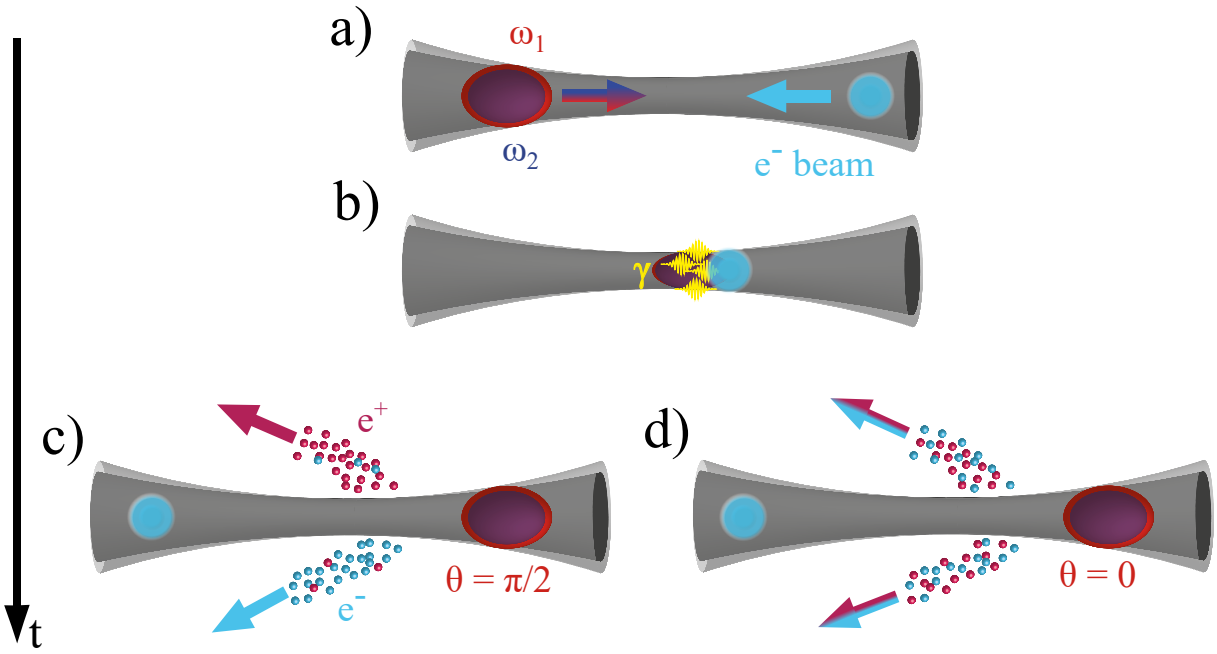

Figure 1.1: Schematic for a charge separation setup. a) an electron beam and two-colored laser pulse are sent in a head-on collision, b) the electrons emit photons due to nonlinear Compton scattering, c) for a phase offset θ of $\pi/2$ between the two colors of the pulse, the electrons and positrons tend to drift in opposite directions, d) for $\theta = 0$, this isn't observed, and each particle is equally likely to drift in any direction.

1.2 Relevant Particle Interactions

1.2.1 Radiation Reaction

All electrically charged particles that undergo changes in their velocity emit electromagnetic radiation. The energy emitted in this radiation comes at the cost of a loss of the particle's kinetic energy. It is, therefore, necessary to account for this loss of energy with a friction-like force when describing the movement of a charged particle. In setups where this radiated energy is small compared to the particle's energy, the movement of charged particles is correctly predicted by applying the Lorentz force $\vec{F_L}$ alone, which is given by

$$\vec{F_L} = q\left(\vec{E} + \vec{v} \times \vec{B}\right) \ , \tag{1.1}$$

where q is the charge of the particle, $\vec{v} = d\vec{r}/dt$ is the velocity of the particle, with $\vec{r}$ its position, and $\vec{E}$ and $\vec{B}$ are the electric and magnetic fields acting on the particle, respectively. The electric and magnetic fields are given for any spatial arrangement of charges by solving Maxwell's equations

$$\vec{\nabla} \cdot \vec{E} = \frac{\rho}{\varepsilon_0} \tag{1.2a}$$

$$\vec{\nabla} \cdot \vec{B} = 0 \tag{1.2b}$$

$$\vec{\nabla} \times \vec{E} = -\frac{\partial \vec{B}}{\partial t} \tag{1.2c}$$

$$\vec{\nabla} \times \vec{B} = \mu_0 \vec{J} + \mu_0 \varepsilon_0 \frac{\partial \vec{E}}{\partial t} \ . \tag{1.2d}$$

where ρ is the charge density, $\vec{J}$ is the current density and ε_0 and μ_0 are the permittivity and permeability of vacuum, respectively. Equation 1.1, dictates how the motion of all charged particles evolves in time, allowing for the calculation of ρ and $\vec{J}$. Meanwhile, with these quantities and equations 1.2, the time evolution of the fields is determined. This is at the heart of all of classical electrodynamics.

However, for cases where the energy losses caused by radiation emission become relevant, the Lorentz force becomes insufficient to correctly predict the motion of charged particles. The electric and magnetic fields of a charged particle with arbitrary motion are given by

$$\vec{E}_{rad} = \frac{q}{4\pi\varepsilon_0} \left[\frac{\vec{n} - \vec{\beta}}{\gamma^2 (1 - \vec{\beta} \cdot \vec{n})^3 R^2} \right]_{ret} + \frac{q}{4\pi\varepsilon_0 c} \left[\frac{\vec{n} \times ((\vec{n} - \vec{\beta}) \times \frac{d\vec{\beta}}{dt}}{(1 - \vec{\beta} \cdot \vec{n})^3 R} \right]_{ret} , \tag{1.3a}$$

$$\vec{B}_{rad} = \left[\frac{\vec{n} \times \vec{E}_{rad}}{c} \right]_{ret} , \tag{1.3b}$$

where $\vec{\beta} = \vec{v}/c$, γ is the Lorentz factor of the particle, $R = |\vec{r} - \vec{r'}| - (\vec{r} - \vec{r'}) \cdot \vec{v}/c$ with $\vec{r'}$ representing the position of the emitting particle, $\vec{n}$ is a unit vector pointing in the direction of observation and the subscript ret means that all the quantities inside the brackets should be calculated at the retarded time $t - |\vec{r} - \vec{r'}|/c$. The second term in equation 1.3a corresponds to a radiation field decaying as $1/R$ and only exists when the particles have an acceleration $d\vec{\beta}/dt$.

A damping force can be calculated by equating the total energy radiated by the fields in equations 1.3 to the work that it performs[21]. The first calculation, for non-relativistic velocities, is the Abraham-Lorentz force $\vec{F}_{AL}$ given by

$$\vec{F}_{AL} = \frac{q^2}{6\pi\varepsilon_0 c^3 m} \frac{d^2\vec{v}}{dt^2} \tag{1.4}$$

which is dependent on the second derivative of the velocity of the particle. The fact that the equation of motion now has a third derivative in time ($d^2\vec{v}/dt^2 = d^3\vec{r}/dt^3$) results in nonphysical "runaway solutions" with arbitrary energy gain. Some solutions were proposed for this problem, but this remains an active field of research [22–25]. The relativistic correction of equation 1.4 is the Dirac-Abraham-Lorentz force F^{μ}_{DAL} given in covariant representation by

$$F^{\mu}_{DAL} = \frac{q^2}{6\pi\varepsilon_0 c^3 m} \left(\frac{d^2 u^{\mu}}{ds^2} - u^{\mu} u^{\nu} \frac{d^2 u_{\nu}}{ds^2} \right) \ . \tag{1.5}$$

where u^{μ} is the velocity 4-vector given by $u^{\mu} = (\gamma c, \gamma \vec{v})$ and s represents the space-time interval, related to τ, the proper time of the particle, by $ds = c d\tau$. One then obtains the equation of motion (also written in covariant form)

$$mc\frac{du^{\mu}}{ds} = qF^{\mu\nu}u_{\nu} + F^{\mu}_{DAL} \ , \tag{1.6}$$

where $F_{\mu\nu}$ is the electromagnetic tensor (the metric diag(+,-,-,-) is used) given by

$$F_{\mu\nu} = \begin{bmatrix} 0 & Ex/c & Ey/c & Ez/c \\ -Ex/c & 0 & -B_z & B_y \\ -Ey/c & B_z & 0 & -B_x \\ -Ez/c & -B_y & B_x & 0 \end{bmatrix} \ , \tag{1.7}$$

with the subscripts x, y and z representing the component of each field in each direction. The first term in equation 1.6 is the Lorentz force, while the second is the radiation reaction. Despite being corrected to relativistic speeds, this equations still has the problem of runaway solutions. One solution proposed by Landau and Lifshitz to get rid of these nonphysical solutions is to use a perturbative expansion to rewrite the second derivative in velocity in terms of velocities contracted with the electromagnetic field. This results in the Landau-Lifshitz radiation reaction F^{μ}_{LL} given by [26]

$$F^{\mu}_{LL} = \frac{q^3}{16\pi\varepsilon_0 mc^2}\left(\frac{\partial F^{\mu\nu}}{\partial x^{\alpha}}u_{\nu}u^{\alpha} - \frac{q}{mc}F^{\mu\nu}F_{\alpha\nu}u^{\alpha} + \frac{q}{mc}F_{\alpha\beta}u^{\beta}F^{\alpha\delta}u_{\delta}u^{\mu}\right) \ . \tag{1.8}$$

This radiation reaction correctly eliminates runaway solutions, however, only with the high intensities of upcoming laser facilities will it be possible to understand how accurately it models the actual radiation damping felt by electric charges. One final approximation made in the present discussion is to neglect the first term in 1.8, which depends explicitly on the derivatives of the electromagnetic field. This approximation is justified since the period of oscillation of the laser pulses used is much greater than the period associated with the frequency of the emitted radiation [24]. Thus, this reduced Landau-Lifshitz radiation reaction F^{μ}_{LLR}, is written as

$$F^{\mu}_{LLR} = \frac{q^4}{16\pi\varepsilon_0 m^2c^4}\left(-\frac{q}{mc}F^{\mu\nu}F_{\alpha\nu}u^{\alpha} + \frac{q}{mc}F_{\alpha\beta}u^{\beta}F^{\alpha\delta}u_{\delta}u^{\mu}\right) \ . \tag{1.9}$$

1.2.2 Nonlinear Compton Scattering

The production of pairs in laser-electron scattering happens in essentially two steps. First, electrons radiate high-energy photons with help of the laser fields, through nonlinear Compton scattering. Those photons then, still in the presence of the intense fields decay into an electron-positron pair via nonlinear Breit-Wheeler pair creation. The sequential and repeated occurrence of these processes results in a QED cascade, which can drastically increase the population of particles in the system.

Nonlinear Compton Scattering is a QED process that results in a charged particle emitting a photon in the presence of a high-intensity electromagnetic field. Only the case where the charged particle is either an electron or a positron is relevant for the present study. Also, the strong fields are considered to be achieved by a high-intensity laser pulse. This process is illustrated in the Feynman diagram shown in figure 1.2 on the right and compared with the regular Compton scattering on the left. Before introducing the rate of this

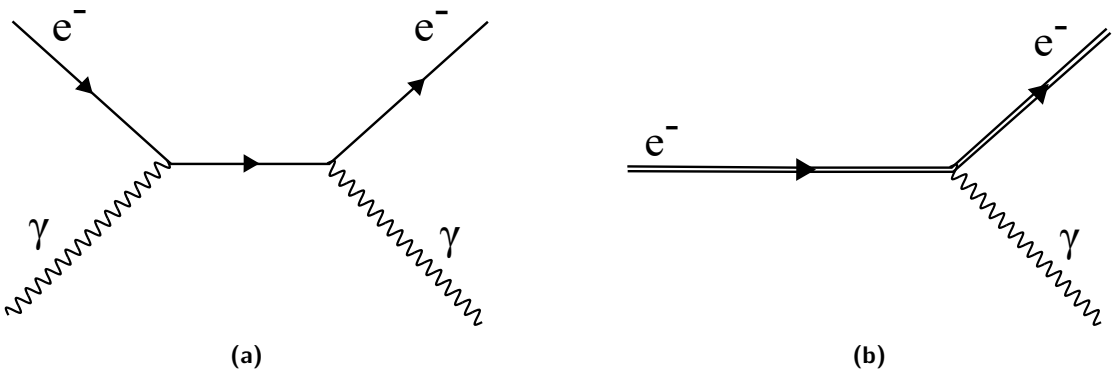

Figure 1.2: Feynman diagrams for a) Compton scattering of an electron and b) nonlinear Compton scattering of an electron. Time evolves from left to right. In image b), fermionic lines have a double stroke to indicate that they are in the presence of a strong background field, according to the Furry picture for QED [27]

process, it is convenient to introduce some Lorentz invariant quantities. One of them is the reduced vector potential a_0 given by

$$a_0 = \frac{eE}{m_e c \omega_0} \tag{1.10}$$

where e is the elementary charge, m_e is the mass of the electron, c is the speed of light in vacuum, ω_0 is the angular frequency of the laser producing the high-intensity field and E is the field's amplitude. The other two important Lorentz invariant quantities are η and χ given by

$$\eta = \frac{\sqrt{|(F_{\mu\nu} p^\mu)^2|}}{E_s m_e} \tag{1.11a}$$

$$\chi = \frac{\sqrt{|(F_{\mu\nu} \hbar k^\mu)^2|}}{E_s m_e} \ , \tag{1.11b}$$

where, p^μ is the momentum 4-vector defined as $p^\mu = (m_e \gamma c, m_e \gamma \vec{v})$, $\hbar$ is the reduced Planck constant, $E_s = m_e^2 c^3 / e\hbar$ is the Schwinger field [28] and k^μ is the wave 4-vector of a photon defined as $k^\mu = (\omega/c, \vec{k})$ with $\vec{k}$ the wavevector associated with the photon with $|\vec{k}| = \omega/c$ and ω the angular frequency of the photon. Nonlinear Compton scattering only occurs in the QED regime, which is only reached when $\eta \sim 1$. For $\eta \ll 1$ and $\chi \ll 1$, the interaction happens in the classical regime, and QED effects are negligible. It is important to highlight the impact of the Schwinger field E_s in these equations. Its value is $\sim 10^{18}$ V/m, while the highest possible electric field reachable with state-of-the-art laser technologies is only around $\sim 10^{15}$ V/m. This would imply that the QED regime is currently unobtainable. However, by using highly relativistic particles, the lack of intensity in $F_{\mu\nu}$ can be compensated with high values of γ in p^μ and ω in k^μ. This way, η and χ can still reach values in the order of 1 with state-of-the-art laser facilities. It's worth mentioning that the expressions for η and χ depend on the geometry of the collision between the laser and the particles. For a head-on collision, the values of these parameters are maximized. However, for co-propagation $\chi, \eta \longrightarrow 0$ and QED phenomena are suppressed.

In the energy regime we are interested, spin effects will not contribute significantly to the behavior of the system, in comparison to the interaction between the particles and the external electromagnetic fields. Therefore we will neglect these proprieties completely and consider only rates for QED processes which are

spin averaged and integrated over all emission angles. The differential rate for nonlinear Compton scattering $d^2N_{nCS}/dtd\chi$ of an electron or positron with parameter χ emitting a photon is then calculated to be [11]

$$\frac{d^2N_{nCS}}{dtd\chi} = 2\sqrt{3}\frac{m_e c^2 \alpha \eta}{h\gamma\chi} F(\chi,\eta) \ , \tag{1.12}$$

with α is the fine structure constant, h is Planck's constant, and the function $F(\chi,\eta)$ is given by

$$F(\chi,\eta) = \frac{2\chi^2}{3\sqrt{3}\pi\eta^4} \sum_{i=1}^{3} F_i(\chi/\eta) J_i(Y) \ , \tag{1.13}$$

with Y, F_i and J_i defined by:

$$Y = \frac{\chi}{3\eta(\eta-\chi)} \ , \tag{1.14a}$$

$$F_1(x) = 1 + (1-x)^{-2} \ , \tag{1.14b}$$

$$F_2(x) = 2(1-x)^{-1} \ , \tag{1.14c}$$

$$F_3(x) = x^2(1-x)^{-2} \ , \tag{1.14d}$$

$$J_1(x) = \frac{1}{3Y^2}\int_Y^\infty du \frac{u}{\sqrt{(u/Y)^{2/3}-1}} K_{2/3}^2(u) \ , \tag{1.14e}$$

$$J_2(x) = \frac{1}{3Y}\int_Y^\infty du \left(\frac{u}{Y}\right)^{1/3} \sqrt{(u/Y)^{2/3}-1} K_{1/3}^2(u) \ , \tag{1.14f}$$

$$J_3(x) = \frac{1}{3Y^2}\int_Y^\infty du \frac{u}{\sqrt{(u/Y)^{2/3}-1}} K_{1/3}^2(u) \ , \tag{1.14g}$$

where K are the modified Bessel functions of the 2nd kind.

This result for the differential rate of photon emission is valid for a constant external field with a very high intensity. Since the intense field comes from a laser in this study, which is oscillatory in nature, this result can only be applied locally for whatever value $F^{\mu\nu}$ has in the moment of the interaction. However, in the approximation $a_0 \gg 1$, as is the case for our lasers, this approximation is justified, since the time scale at which the electrons deflect is much slower than the intensity of the laser changes [29]. A plot of this rates as a fraction of the energy imparted to the photon is present in figure 1.3 for some values of η. From this plot, it is visible that most of the photons being generated are of very low energy, but the high energy photons carry most of the radiated energy.

1.2.3 Nonlinear Breit-Wheeler Pair Emission

The other predominant QED process that is relevant in laser-beam interaction is the nonlinear Breit-Wheeler pair creation. In this process, an energetic photon in the presence of an intense electromagnetic field decays into an electron-positron pair. The Feynman diagram governing this process is seen in figure 1.4 on the right, while the diagram on the left represents its linear counterpart, which remains to be experimentally verified, due to the difficulty of colliding high energy photons with a density large enough for the process to be seen [12]. However, for the nonlinear case, since the strong electromagnetic field mediates the process, this problem is surpassed, and the energetic photons arising from nonlinear Compton scattering can, in the presence of the same laser, decay into pairs.

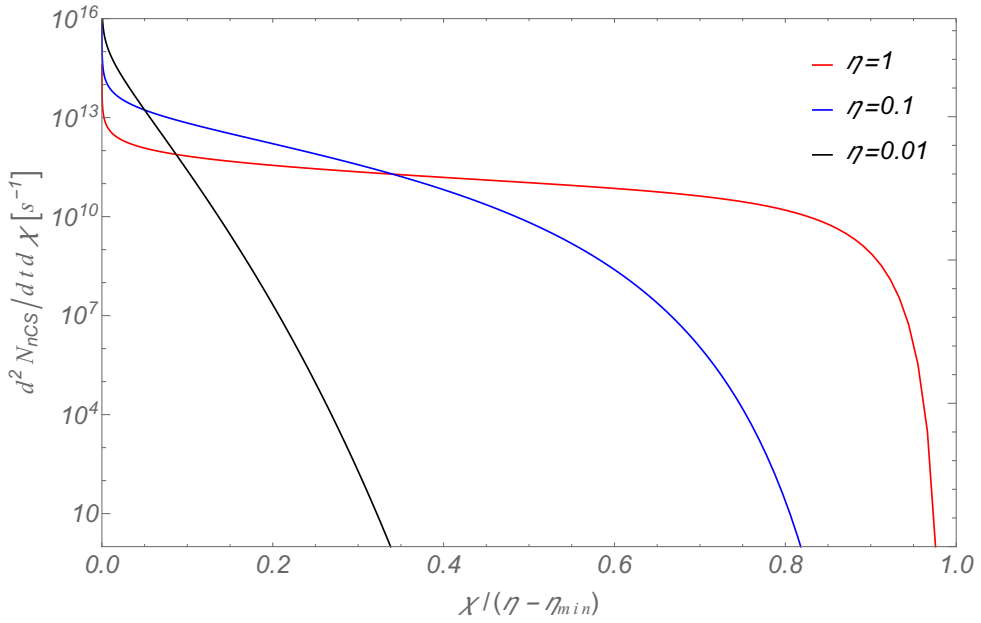

Figure 1.3: Plot of the differential rate of nonlinear Compton scattering as a function of the fraction of energy that the photon can take from electrons with η of 0.001, 0.1, and 1. η_{min} corresponds to setting $\gamma = 1$ in equation 1.11a.

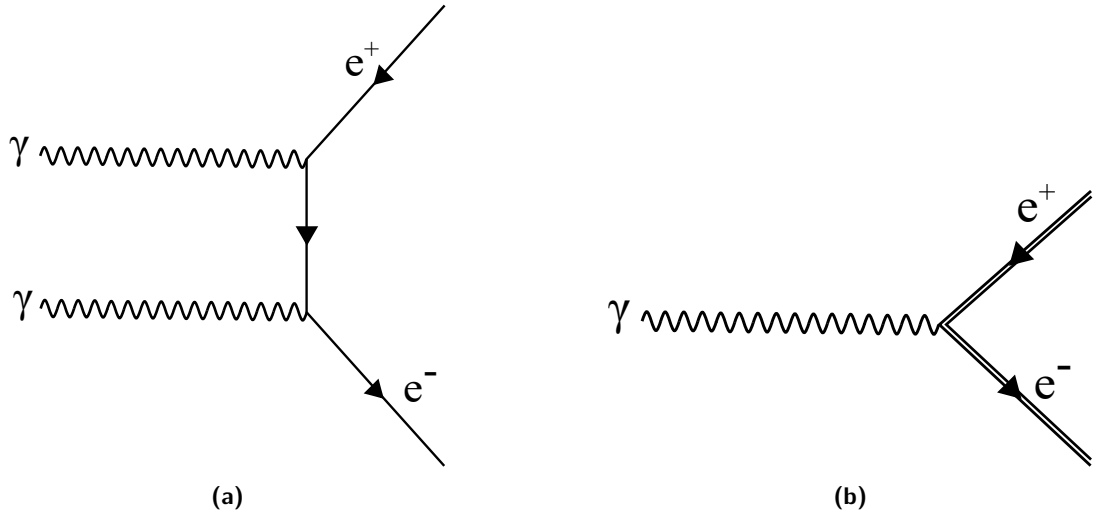

Figure 1.4: Feynman diagrams for a) Breit-Wheeler pair creation and b) nonlinear Breit-Wheeler pair creation. Time evolves from the left to the right. Image b) is, once again, in the presence of a strong background field.

The differential rate for a photon with angular frequency ω decaying into a pair via this process can be written, once again, as a function of the parameters χ and η as (spin averaged and integrated for all emission angles)

$$\frac{d^2 N_{nBW}}{dtd\eta} = \frac{\alpha m_e^2 c^4}{\sqrt{3}\pi\hbar^2\omega\chi}\left[\left(\frac{\xi^+}{\xi^-}+\frac{\xi^-}{\xi^+}\right)K_{2/3}(\hat{\chi}) + \int_{\hat{\chi}}^{\infty} dx K_{1/3}(x)\right] \tag{1.15}$$

where $d^2 N_{nBW}/dtd\eta$ is the differential rate for nonlinear Breit-Wheeler pair creation, and the auxiliary quantities ξ^+, ξ^- and $\hat{\chi}$ are given by

$$\hat{\chi} = \frac{2}{3\chi\xi^+\xi^-} \,, \tag{1.16a}$$

$$\xi^+ = 1 - \xi^- = \frac{\eta}{\chi} \,. \tag{1.16b}$$

A plot of this differential rate is given in figure 1.5 for some values of χ, in it, it is possible to see that this function is symmetric. This behavior would be expected, since a photon should have no preference in distributing its energy to an electron or positron, since they have the same mass. Therefore, the probability of creating a lepton with a fraction of energy η/χ has to be the same as the probability of creating it with a fraction $1 - \eta/\chi$. It is also visible that as χ increases, it becomes more likely for one particle to carry most of the energy.

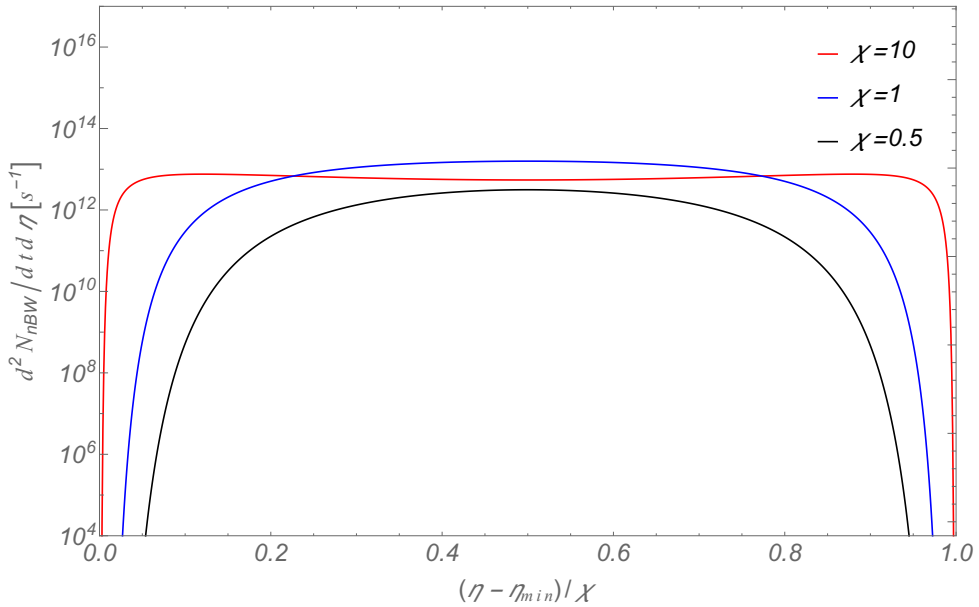

Figure 1.5: Plot of the differential rate of nonlinear Breit-Wheeler pair creation as a function of the fraction of energy that an electron (or positron) takes from a photon with χ of 0.5, 1, and 10.

Focusing on the total rate of pair creation dN_{nBW}/dt, given by integrating the previous quantity over all possible values of η of the created pairs, the total rate is

$$\frac{dN_{nBW}}{dt} = \int_{\eta_{min}}^{\chi-\eta_{min}} \frac{d^2 N_{nBW}}{dt\,d\eta}\, d\eta \,, \tag{1.17}$$

where η_{min} is obtained by setting γ to 1 in equation 1.11a, i.e., saying the pairs are produced at rest and have only their rest mass energy. Once again, the use of equations 1.15 and 1.17 follows the assumption that the local values of the electromagnetic field are a static background field, which is justified for high a_0 values [29].

1.3 Particle-in-Cell Codes

1.3.1 Particle-in-cell Algorithm

Particle-in-Cell (PIC) [30] codes are, due to their the ease in being implemented with massive parallel computing, an extremely useful tool for simulation in plasma physics [20, 31]. The main mechanism behind the PIC method that turns it into a very efficient simulation tool consists in calculating the electric and magnetic fields only in a spatially discretized grid. Normally, in a system with $N \gg 1$ particles, to account for all interactions among them would scale with $N(N-1) \approx N^2$ computations, since this is the amount of possible interactions between 2 particles. However, depositing an electric field on the grid, and then extrapolating the forces on the particles from these fields scales only with N computations. This is ideal when scaling the simulation for high values of N. These particles are evolved in time according to the Lorentz force in equation 1.1. Particles, however, live in full 3D space, so in order to know the field values in their location, an interpolation of the fields to their position is made. After pushing the particles, a new current density $\vec{J}$ is deposited on the grid points and a new value for the electric and magnetic fields is calculated by solving Faraday's law (equation 1.2c) and Ampere's law (equation 1.2d). A flowchart of the algorithm can be seen in figure 1.6.

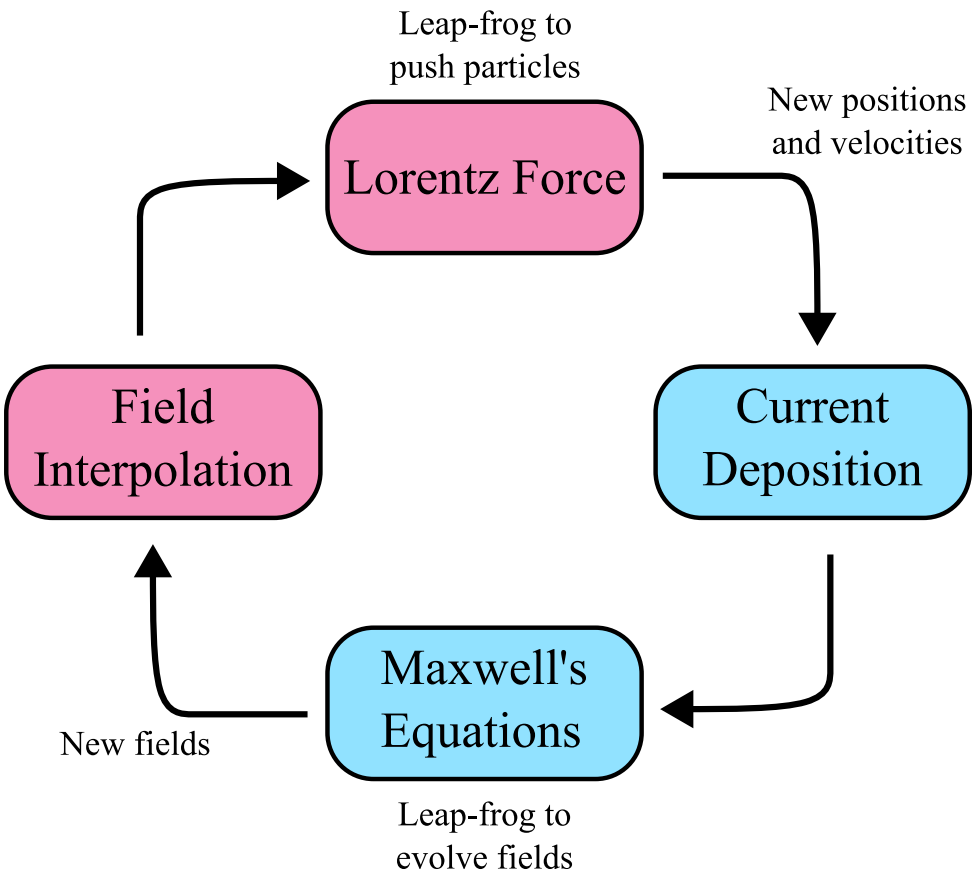

Figure 1.6: Flowchart of the algorithm in conventional PIC codes. The blue boxes represent algorithms occurring in the grid points and in pink the computations in full 3D space.

Macroparticles

The first thing to consider when approaching a PIC code is that, despite the reduction of operations by using a grid to mediate the forces, it is still unfeasible to simulate the same number of particles as in a real plasma (which can is on the order of 10^{20} particles/cm^3). Therefore, particles are instead clumped into macroparticles. A macroparticle is a particle that represents a large number of real particles that are intended to be simulated. The macroparticles carry the total mass, charge, and energy of the particles that it simulates. A macroparticle also occupies a finite size, instead of being represented by a point. This has the advantage of avoiding the divergences characteristic of the Coulomb interaction near the particle's center ($E \sim 1/r^2$). Particles live in finite-sized cells and represent a volume on the order of a cell size with a certain charge density. Each cell may also contain more than one macroparticle and a down-sampled momentum distribution. This gives rise to an important parameter in the simulations which is the number of particles per cell. The more particles per cell there are, the more accurate the description of momentum space of the macroparticles is.

Field Interpolation

The interpolation of the electric and magnetic fields happens according to a weighted average of the grid points in the vicinity of the particle's position. In 2D, normally the grid forms a rectangular lattice, where a cell has the shape of a rectangle. In this case, the field is just determined by weighting each field with the area that is closer to each part of the cell (see the bottom left part of figure 1.7). Calling the area that's closer to the field E_1 and its area A_1, and similarly for the other 3 fields, results in a field in the center of the particle E_{part} given by

$$E_{part} = \frac{E_1 A_1 + E_2 A_2 + E_3 A_3 + E_4 A_4}{A_1 + A_2 + A_3 + A_4} \ . \tag{1.18}$$

Particle Pusher

After knowing the fields in the positions of the particles, the Lorentz force acting on each particle advances it in time. A method suggested by Boris [32] allows for higher accuracy in time evolution. For this, the positions are defined for each step x^n, and the velocities are defined in the intermediate steps $v^{n+\frac{1}{2}}$. With the relativistic equation of motion

$$\frac{d(\gamma \vec{v})}{dt} = \frac{q}{m}\left(\vec{E} + v \vec{\times} \vec{B}\right) \ , \tag{1.19}$$

the particles are then evolved as such (variables with primes are just auxiliary):

1. Use half of the electric force term in Lorentz force

$$\gamma' \vec{v}' = \gamma^{\,n-\frac{1}{2}} \vec{v}^{\,n-\frac{1}{2}} + \frac{q \Delta t \vec{E}^n}{2m} \tag{1.20}$$

with Δt the time step of the simulation;

2. With this, calculate an estimate for $\gamma' = \sqrt{1 + (\gamma' v')^2}$ and $\vec{v}' = \gamma' \vec{v}'/\gamma'$;

3. Using γ', advance half of the magnetic rotation

$$\gamma'' \vec{v}'' = \gamma' \vec{v}' + \frac{q \Delta t \vec{v}' \times \vec{B}^n}{2m} \; ; \tag{1.21}$$

4. Perform the full rotation to this estimate and add to the initial one $\gamma' \vec{v}'$ (and assuring that the velocity is kept constant after the rotation, hence the denominator in the next equation)

$$\gamma''' \vec{v}''' = \gamma' \vec{v}' + \gamma'' \vec{v}'' \times \frac{2 \frac{q \Delta t \vec{B}^n}{2m}}{1 + \left(\frac{q \Delta t \vec{B}^n}{2m} \right)^2} \; ; \tag{1.22}$$

5. Finally, adding the remaining $\vec{E}$ half step

$$\gamma^{\,n+\frac{1}{2}} \vec{v}^{\,n+\frac{1}{2}} = \gamma''' \vec{v}''' + \frac{q \Delta t \vec{E}^n}{2m} \; . \tag{1.23}$$

After all this, $\gamma^{\,n+\frac{1}{2}}$, $\vec{v}^{\,n+\frac{1}{2}}$ and $\vec{r}^{\,n+1}$ are calculated by doing

$$\gamma^{n+\frac{1}{2}} = \sqrt{1 + (\gamma^{n+\frac{1}{2}} v^{n+\frac{1}{2}})^2} \; , \tag{1.24a}$$

$$\vec{v}^{\,n+\frac{1}{2}} = \frac{\gamma^{\,n+\frac{1}{2}} \vec{v}^{\,n+\frac{1}{2}}}{\gamma^{\,n+\frac{1}{2}}} \; , \tag{1.24b}$$

$$\vec{r}^{\,n+1} = \vec{r}^{\,n} + \vec{v}^{\,n+\frac{1}{2}} \Delta t \; . \tag{1.24c}$$

Current Deposition

After the movement of the particles is updated, the electric current in the positions of the the cells is calculated. However, it is required to interpolate these values to the grid, since that's where the fields are defined. To do this, a calculation of the amount of charge passing through the boundaries of the cells is performed (see top right part of figure 1.7). The exact formula for this depends on how many boundaries the cells cross, but the concept remains the same.

Field Evolution

After having the current, Maxwell's equations are used to evolve the fields in time. Namely, the ones who give the time evolution of the fields are

$$\frac{\partial \vec{B}}{\partial t} = -\vec{\nabla} \times \vec{E} \; , \tag{1.25a}$$

$$\frac{\partial \vec{E}}{\partial t} = \frac{\vec{\nabla} \times \vec{B}}{\varepsilon_0 \mu_0} - \frac{\vec{J}}{\varepsilon_0} \; . \tag{1.25b}$$

Finite differences can be used to evaluate the curls present in these equations. To increase spatial accuracy in these curls, the various components of each vectorial field are defined in grids with some offsets. Also, to increase time accuracy, the currents are defined for $\vec{J}^{n+\frac{1}{2}}$, while the electric and magnetic field are defined for

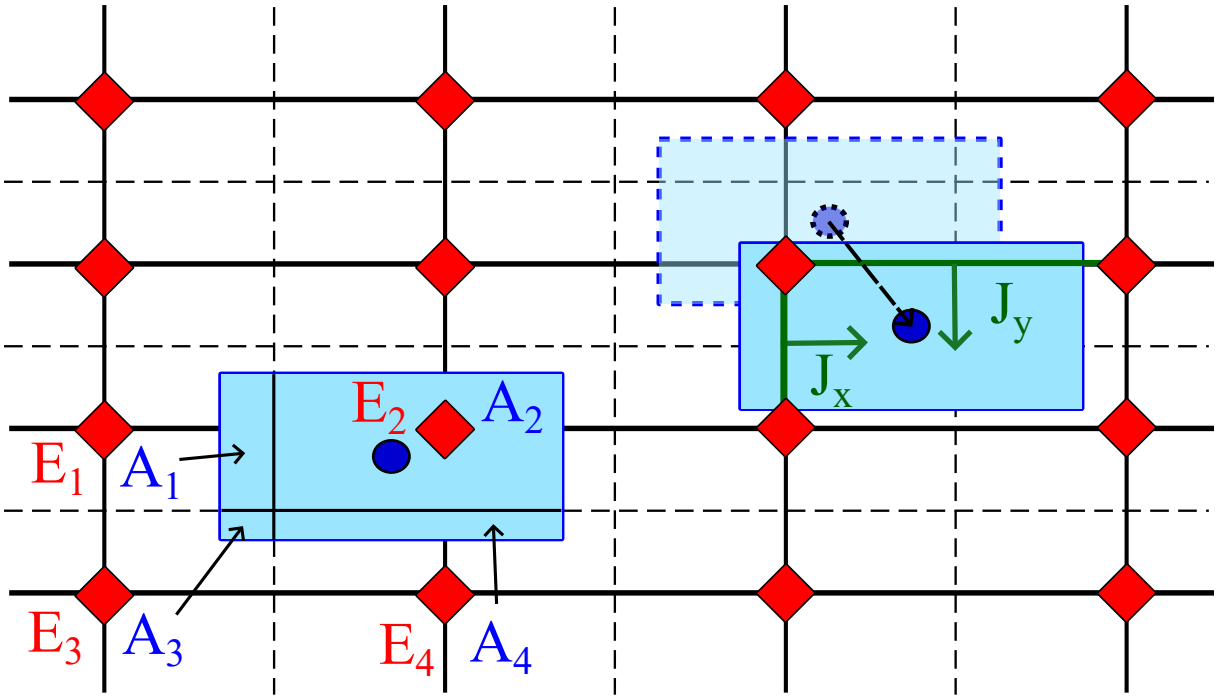

Figure 1.7: Schematic for the field interpolation (bottom left) and current deposition (top right) for a simple PIC algorithm.

times $\vec{E}^n$ and $\vec{B}^n$. The evolution of the fields and the current in time is then done with a leap-frog algorithm quite similar to the one used for pushing the particles by 1) advancing $\vec{B}$ half a timestep; 2) advancing $\vec{E}$ a full time step and 3) advancing $\vec{B}$ the remaining half timestep.

1.3.2 OSIRIS QED

For this thesis, all PIC simulations are done using the OSIRIS framework, which is a massively parallel fully relativistic PIC code [18]. This code uses the algorithms presented in the previous section to advance the electric and magnetic fields, as well as particle positions and velocities in time. However, in the QED regime, some alterations have to be added to the code to correctly account for these phenomena. Radiation reaction must be included to the motion of the particles [25]. This happens because, in the presence of intense laser fields, particles undergo very rapid accelerations on the timescale of the oscillation of the laser. This acceleration produces some radiation, as discussed previously, and causes the particle to lose energy. In the regime where nonlinear Compton scattering is still not a dominant process ($\eta \lesssim 1$), radiation reaction can be approximated to the expression given in equation 1.9. With this in mind, the addition of this force to the Lorentz force in the particle pusher corrects the movement for radiation reaction, since the Landau-Lifshitz radiation reaction does not produce runaway solutions. In regimes where nonlinear Compton scattering becomes a relevant phenomenon, the paradigm in the simulation must change.

First, the code loops over all charged particles in the simulation. If their η parameter is small, then the reduced Landau-Lifshitz radiation reaction is simply added to the equation of motion, as stated above. Otherwise, a Monte-Carlo algorithm determines, according to equation 1.12 if a photon is emitted or not by

the particle [20]. In case the particle does emit a photon, then energy is removed from the emitting particle equaling the one that the photon carried away. This way, a stochastic radiation reaction that only occurs in the presence of photon emission in the corresponding time step is achieved. The photon that is emitted is only added to the photon pusher (which is a separate pusher than for charged particles) in case its energy is above a threshold which is chosen to be $2m_e c^2$. This is done to not overload the pusher with photons that would never be able to produce an electron-positron pair. This is particularly useful since nonlinear Compton scattering produces a very large amount of low-energy photons (see figure 1.3).

After this, the simulation has energetic photons that free-stream in time in a straight line until they decay into pairs (due to the interaction with a strong background field). Therefore, another Monte-Carlo algorithm loops over all photons in the simulation to calculate if they emit an electron-positron pair or not. This algorithm uses the differential rate of the nonlinear Breit-Wheeler pair creation from equation 1.15 [20]. This results in the emission a positron and an electron, moving in the direction the photon was initially moving, in such a way that momentum is conserved (recall the symmetry in figure 1.5). The photon is also destroyed and removed from the simulation. The new pair is now added to the particle pusher, also subject to more QED effects and radiation reaction. A flowchart with the algorithm can be seen in figure 1.8.

OSIRIS is coded, as most PIC codes, in plasmas units. This allows better precision since a good amount of numeric factors are no longer present in these units and quantities are of the same order of magnitude. Therefore, with primed variables representing the value of that variable in plasma units, they are related to their value in SI units by

$$t' = t\omega_p \ , \tag{1.26a}$$

$$v' = v\frac{1}{c} \ , \tag{1.26b}$$

$$x' = x\frac{\omega_p}{c} \ , \tag{1.26c}$$

$$m' = m\frac{1}{m_e} \ , \tag{1.26d}$$

$$\epsilon' = \epsilon\frac{1}{mc^2} \ , \tag{1.26e}$$

$$q' = q\frac{1}{e} \ , \tag{1.26f}$$

$$E' = E\frac{m_e c\omega_p}{e} \ , \tag{1.26g}$$

$$B' = B\frac{m_e\omega_p}{e} \ , \tag{1.26h}$$

where ϵ is the energy of a particle and ω_p is the plasma frequency given by

$$\omega_p = \sqrt{\frac{n_e e^2}{\varepsilon_0 m_e}} \tag{1.27}$$

and n_e is the critical density of the plasma, to which all densities are normalized.

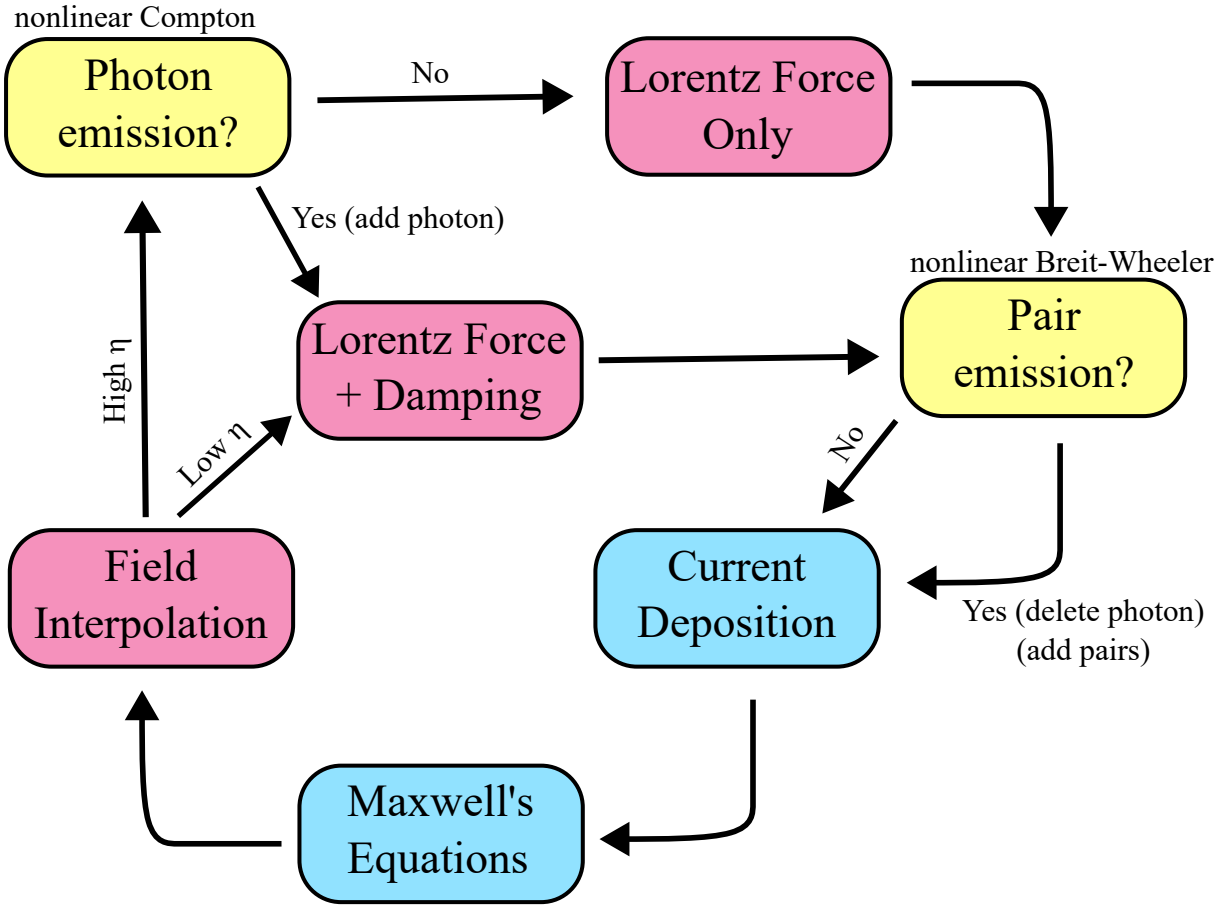

Figure 1.8: Flowchart of the algorithm in OSIRIS with QED module. The yellow boxes correspond to Monte Carlo calculations. "Damping" is either according to the reduced Landau-Lifshitz equation for low η particles, or QED corrected for high η. Photons are only added if they have an energy higher than $2mc^2$.

Chapter 2

Analytical Study of Electron-Seeded Pair Generation in Two-colored Pulses - Ideal Description (Plane Wave)

2.1 Motion in Two-colored Pulses

I consider, as shown in the setup on figure 1.1, that a relativistic electron beam collides with a two-colored laser pulse. In the present study, the high-intensity laser is composed by the sum of two waves, where the second is the second harmonic of the first. An expression for the field is, therefore, for linearly polarized waves (assuming propagation along the z axis and polarization in the x axis)

$$\vec{E} = E_1 \cos(\phi)\vec{e_x} + E_2 \cos(2\phi + \theta)\vec{e_x} \ , \tag{2.1}$$

where E_1 and E_2 are the amplitudes of the 1st and 2nd harmonic fields, respectively, ϕ is the phase of the wave given by $\phi = \omega_0 t - k_0 z$ with ω_0 the angular frequency and $k_0 = \omega_0/c$ the wavenumber of the first harmonic, θ is an offset phase between both harmonics and $\vec{e_x}$ is a unit vector pointing in the x direction. In this section, I consider both harmonics as plane waves, however, in Chapter 3, the simulations are performed with pulses with finite size and duration.

Since the motion of the electrons and positrons is relativistic, Newton's 2nd law must be solved for the relativistic motion of these particles under the Lorentz force. A correct description would require the addition of a radiation reaction force. However, in this section, for simplicity, only the case of negligible radiation damping is discussed. Despite affecting the motion of the particles, the qualitative presence of a net current in the transverse direction shouldn't be altered, since radiation damping acts similarly to a drag force and wouldn't be able to swap the direction of drift of a particle. The equations of motion are then written as

$$\frac{d\gamma\beta_x}{dt} = \frac{qE_x}{mc}(1-\beta_z)\ , \tag{2.2a}$$
$$\frac{d\gamma\beta_y}{dt} = 0\ , \tag{2.2b}$$
$$\frac{d\gamma\beta_z}{dt} = \frac{qE_x}{mc}\beta_x\ , \tag{2.2c}$$
$$\frac{d\gamma}{dt} = \frac{qE_x}{mc}\beta_x\ . \tag{2.2d}$$

From the equations, it is possible to conclude the conservation of two quantities

$$\gamma(1-\beta_z) = \text{const}\ , \tag{2.3a}$$
$$\gamma\beta_x + \frac{qA_x}{mc} = \text{const}\ , \tag{2.3b}$$
$$\tag{2.3c}$$

with $\mathbf{A}$ being the vector potential satisfying $\mathbf{E} = -\partial\mathbf{A}/\partial t$ and here given by

$$\mathbf{A} = -\frac{E_1}{\omega_0}\sin(\phi)\mathbf{e_x} - \frac{E_2}{2\omega_0}\sin(2\phi+\theta)\mathbf{e_x}\ . \tag{2.4}$$

This alongside with the definition of Lorentz factor $\gamma = (1-\beta^2)^{-1/2}$ allows me to calculate the final velocity of a particle born somewhere along the pulse. This analysis is also valid for a pulse whose envelope varies very slowly in time, in comparison with the temporal variation associated to the oscillating fields. With this in mind, assuming pairs are born moving only in the z direction (the angle of emission will depend on $1/\gamma$, which for highly relativistic particles, allows us to neglect it) with velocity $v_{0z} = \beta_{0z}c$, the final drift velocity (after leaving the pulse, $A_x = 0$), represented by v_{drift} in the x direction is given by

$$v_{drift} = \frac{q}{|q|}\frac{2\gamma_0(1-\beta_{0z})a_1(\sin\phi_0 + \frac{E_2}{2E_1}\sin(2\phi_0+\theta))c}{1+\gamma_0^2(1-\beta_{0z})^2 + a_1^2(\sin\phi_0 + \frac{E_2}{2E_1}\sin(2\phi_0+\theta))^2}, \tag{2.5}$$

where ϕ_0 is the phase at which the particle is born and $a_1 = eE_1/mc\omega_0$. This velocity describes how fast the electrons and positrons drift in the polarization direction after they leave the pulse. It is important to highlight that v_{drift} has an opposite sign for positrons and electrons, which means that they drift at the same rate in opposite directions. The opposite-sign drift velocity could ultimately result in a spatial separation of the charges.

2.2 Pair Production in Two-colored Pulses

The electrons of the beam emit some photons via nonlinear Compton scattering, which then decay into pairs via nonlinear Breit-Wheeler pair creation, as illustrated in figure 1.1. Since the particles are highly relativistic, conservation of momentum dictates that in the photon emission, the particles emit the photons in the direction of motion. Also, the photons decay into an electron-positron pair, partitioning their momentum into two parts.

For a head-on collision along the z-axis, for the case of an electron or positron with Lorentz factor γ, the

momentum four-vector is $p^\mu = (\gamma c, 0, 0, \gamma v_z)$ with $v_z < 0$. For the case of a photon with angular frequency ω, analogously, $k^\mu = (\omega/c, 0, 0, -\omega/c)$. With these 4-vectors, equations 1.11 can be simplified to

$$\eta = 2\,\frac{|E|}{E_s}\,\gamma\ , \tag{2.6a}$$

$$\chi = 2\,\frac{|E|}{E_s}\,\frac{\hbar\omega}{mc^2}\ . \tag{2.6b}$$

where $|E|$ is the instantaneous total electric field.

The electric field is modeled in equation 2.1. Therefore I can replace its expression to determine how η and χ depend on ϕ

$$\eta = 2\gamma\frac{|E_1\cos(\phi) + E_2\cos(2\phi+\theta)|}{E_s}\ , \tag{2.7a}$$

$$\chi = 2\frac{\hbar\omega}{mc^2}\frac{|E_1\cos(\phi) + E_2\cos(2\phi+\theta)|}{E_s}\ . \tag{2.7b}$$

Since I have an expression for χ, η and v_{drift} of the pairs being born, I can estimate the total current being produced by averaging the drift velocity of each particle with the Breit-Wheeler pair creation rate, which will determine in which phases it is most likely for a photon to decay into a pair, and ultimately give rise to an asymmetry in the drift of the species, turning the production of an accumulated current I_{acum} possible, and given by

$$I_{acum} = \frac{2q}{c}\int_0^{2\pi}\int_{\eta_{min}}^{\chi-\eta_{min}} v_{drift}\frac{dN_{nBW}}{dtd\eta}d\eta d\phi_0\ . \tag{2.8}$$

This quantity accounts not only for the fact that some phases produce a higher drift velocity, but also that there are some phases where pair creation is more likely, giving therefore an estimate of the current dependency on ϕ_0. It is worth mentioning that equation 2.8 has no information on the spectrum of photons, and assumes a mono-energetic photon bunch decaying into pairs. This is an approximation that should bear good results when considering the critical photon frequency ω_{crit}, which corresponds to the characteristic energy carried by each photon, and defined according to the condition

$$\int_0^{\omega_{crit}}\omega\frac{dN}{dE}d\omega = \frac{1}{2}\int_0^{\omega_{cutoff}}\omega\frac{dN}{dE}d\omega\ , \tag{2.9}$$

with dN/dE the energy distribution of the photon spectrum and ω_{cutoff} the maximum frequency that a photon can have (assuming it removes all the kinetic energy from a lepton). This quantity can be calculated numerically assuming we know the photon distribution.

Chapter 3

Full-Scale Particle-in-Cell Study of Electron-Seeded Pair Generation in Two-Colored Laser Pulses

Finite Laser Size Effects and Species Separation

3.1 Benchmarking the Analytical Predictions in a Plane Wave-Like Simulation Environment

First, I test (in the approximation of a plane wave) how changing θ and the ratio between the fields E_2/E_1 affects the amount of generated current. This allows me to determine if in fact we should keep $\theta = \pm\pi/2$, as observed for the ionization scenario. It also allows to determine if there is an optimal ratio E_2/E_1 for current production. Therefore, I use OSIRIS to perform 2D simulations in which I initialize the two overlapping plane waves discussed in the previous chapter, where the second harmonic has a phase offset of θ. This laser is then sent to collide against a photon bunch. The laser and the photons are initialized moving in the positive and negative $x1$ direction respectively. The x_2 direction is set to have periodic boundary conditions, which allows for a representation of an infinite plane wave in the x_2 direction. The laser envelope has the profile in x_1 given by the polynomial $p(\delta)$

$$p(\delta) = 10\delta^3 - 15\delta^4 + 6\delta^5 \ , \tag{3.1}$$

where $\delta = (x_1 - x_{start})/c\tau_{rise}$ with x_{start} the starting position of the pulse and τ_{rise} the rise time of the pulse. This function goes from 0 to 1 during τ_{rise} and afterward, the same polynomial is used to go back to 0 in a time τ_{fall} which I take as $\tau_{fall} = \tau_{rise}$. The photon bunch has a uniform density and has an energy distribution given by the quantum synchrotron spectrum (following distribution in equation 1.12) of a mono-energetic electron in a constant field. A table with the simulation parameters is present in table 3.1

and an example of an output from OSIRIS can be seen in figure 3.1

Variable	Value
ω_0	$\approx$ 1.9 x10^{15} Hz
a_1	300
E_2/E_1	{0, 1/3, 2/3, 1, 4/3, 5/3, 2, 3}
θ	{0, $\pi/4$, $\pi/2$, $3\pi/4$, π, $5\pi/4$, $3\pi/2$, $7\pi/4$}
$\tau_{rise} = \tau_{fall}$	$\approx$ 32 fs
Number of cells	4800 x 320
Box size	$\approx$ 70 x 10 μm
Δt	$\approx$ 2.6 as
Radiation Reaction	Off
nonlinear Compton scattering	Off
nonlinear Breit-Wheeler pair creation	On
Particles per cell	2 x 2
Photon density	$\approx$ 1.4 x10^{27} m^{-3}
Photon bunch thickness	$\approx$ 3 μm
Synchrotron spectrum γ	10000
Synchrotron spectrum χ	0.5
$\hbar\omega_{crit}$	1.25 GeV

Table 3.1: Simulation parameters for the simulations. Only E_2/E_1 and θ were varied.

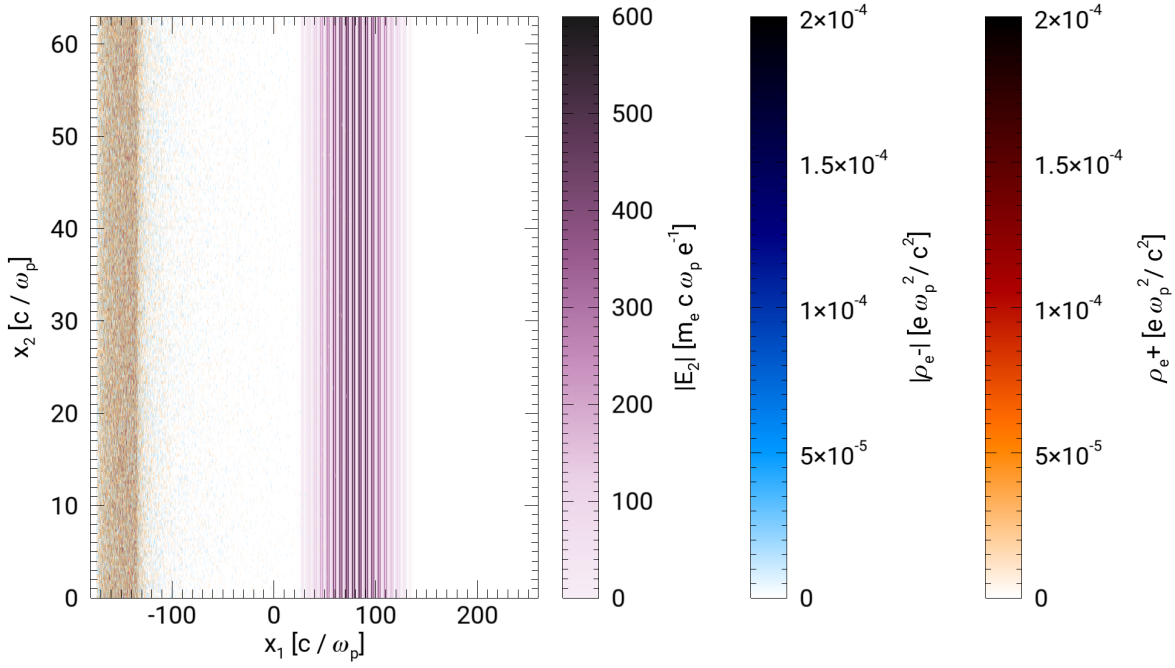

Figure 3.1: Output from an OSIRIS run where a two-colored laser pulse (in purple) moving to the right has collided with a photon bunch (moving to the left and suppressed in the figure for simplicity), which made electrons (in blue) and positrons (in orange) to appear due to nonlinear Breit-Wheeler pair creation. Simulation with $E_2/E_1 = 1$ and $\theta = \pi/2$.

Variation with θ

I start by discussing the results obtained when changing θ. For these runs, E_2/E_1 was kept at 1. In these simulations, there can be no transverse charge separation by construction, so electrons and positrons, produced in the same number, have exactly the same distributions in figure 3.1. However, according to the conclusions of chapter 2, there should be a drift current whose origin lies in the different transverse momentum direction of the species. To observe if this is the case, the distributions of the transverse momentum of electrons and positrons are shown in figure 3.2. In these plots, it is possible to observe that for the phase offsets of $\theta = 0$ and $\theta = \pi$, the distribution of both species is quite similar, with only minor changes near $p_2 = 0$. This results in no net current being produced by the movement of these charges. However, for $\pi = \theta/2$, it is possible to see that these distributions differ, with a dominance of positive momentums for electrons and negative momentums for positrons. This results in a net current in the negative $x2$ direction. Also, for the case of $\theta = 3\pi/2$, a similar separation in momentum space is observed, but in the opposite direction. This would give rise to a current of similar amplitude, but opposite direction. It is worth noting that for $\theta = 0$ and $\theta = \pi$ particles still have a transverse drift velocity, however, both species drift symmetrically in the positive and negative $x2$ direction, so no net current is produced.

To conclude what is the optimal phase offset, the data for the transverse current was gathered for simulations with 8 different values of θ, and a plot of $J2$ as a function of $x1$ is made, for the end time of the simulation. To obtain $J2$ as a function only of $x1$, an averaging of the data over $x2$ is performed. This is physically justifiable since the $x2$ direction is periodic and the plane wave and photon bunches, therefore, have no dependency in $x2$. A plot of the currents for all values of θ is presented in figure 3.3.

From figure 3.3 it can be seen that the tendency for the produced current to evolve as θ changes is to

- Increase for $0 < \theta < \pi/2$;
- Decrease towards 0 for $\pi/2 < \theta < \pi$;
- Increase in the opposite direction for $\pi < \theta < 3\pi/2$;
- Decrease back towards 0 for $3\pi/2 < \theta < 2\pi$.

In order to see if the theoretical model from equation 2.8 correctly predicts this behavior, a comparison of the total integrated current and the output of equation 2.8 are shown for photon energies close to $\hbar\omega_{crit}$ as a function of θ are shown in figure 3.4, where the simulation points have been re-scaled to match the maximum value at $\pi/2$ from the theoretical predictions. From here, I can conclude that despite not being able to give correct estimates for the values of the current (due to different energies in the system), the theoretical description of chapter 2 captures all the main features of the dependency of the charge separation as a function of the phase offset between the laser harmonics for various values of photon energy close to $\hbar\omega_{crit}$. Finally, I verify that this increase in current is in fact due to the variation of θ and not due to an increase of pairs in the system, I present the ratio of the number of pairs and the initial number of photons in the simulation N_{pairs}/N_γ in table 3.2 alongside the values for the integral of the current density of figure

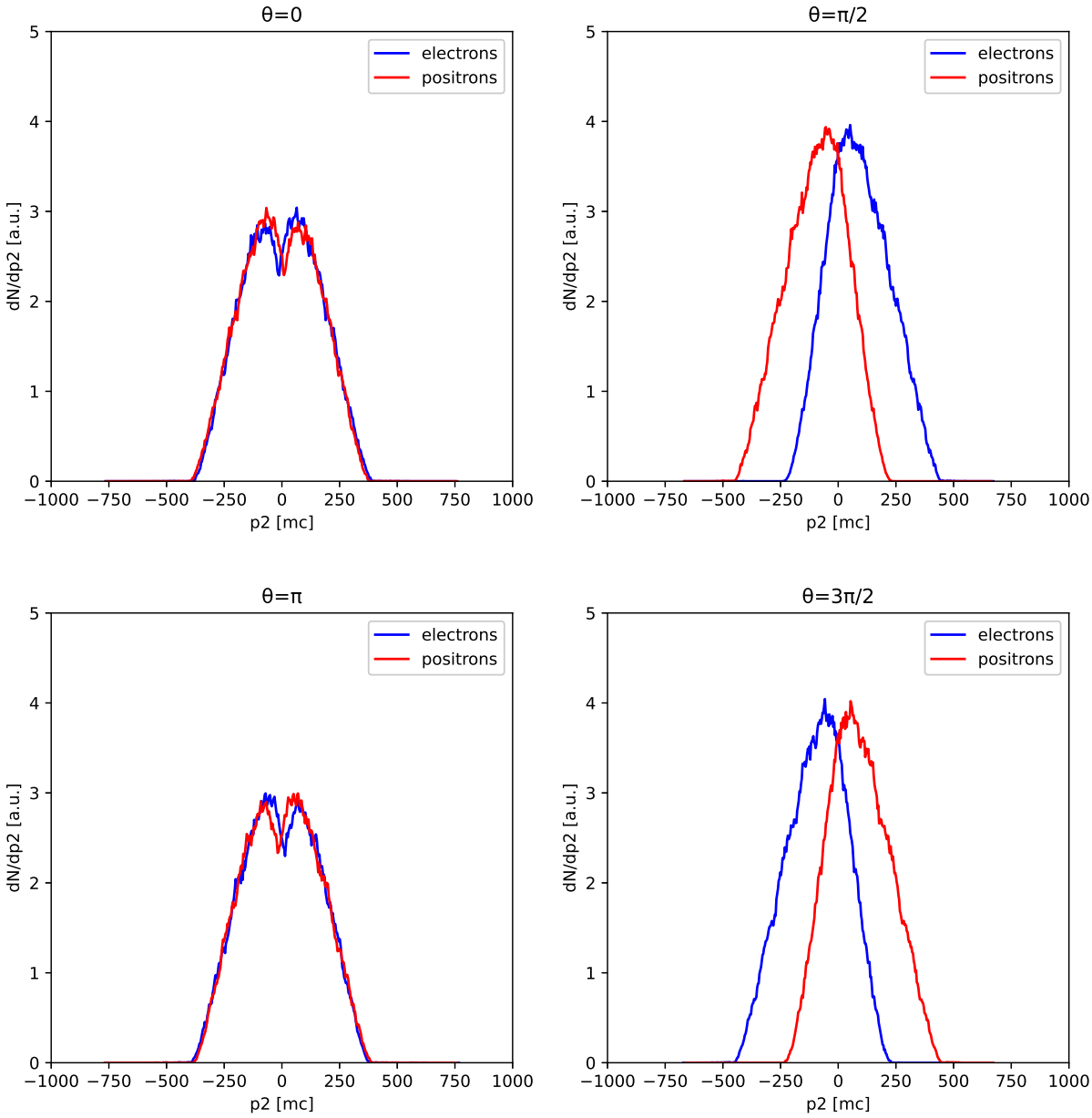

Figure 3.2: Plots of transverse momentum distribution dN/dp_2 for electrons (blue) and positrons (red) in various for values of θ 0, $\pi/2$, π and $3\pi/2$.

3.3. In this table, it is possible to see that the variation in pair number is the order of 2%, while the current changes by more than an order of magnitude, which allows us to conclude that the gain in current is solely due to θ.

Variation with E_2/E_1

Similarly to the study for θ, I now change E_2/E_1 for a fixed value of θ, which is chosen to be $\pi/2$, since it maximizes the produced current. Analogously to the previous simulations, the momentum distributions of the produced pairs for some values of E_2/E_1 are given in figure 3.5. In these distributions, it can be seen that:

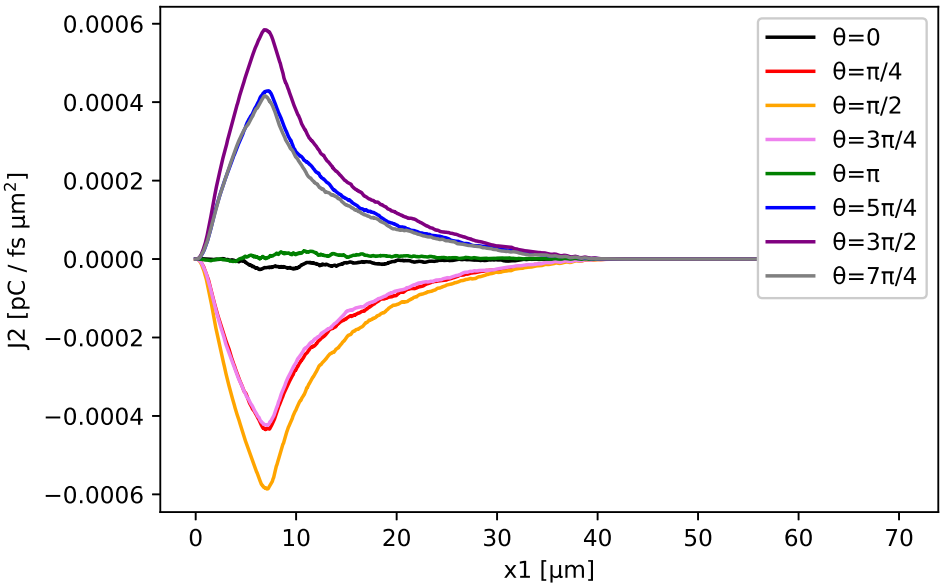

Figure 3.3: Current density $J2$ as a function of $x1$ at the end of the simulation for all the values of θ simulated. $J2$ was first averaged over $x2$, in order to depend only of $x1$. Then, a moving average with a window of 100 points has been performed to remove noise from the output of the simulation.

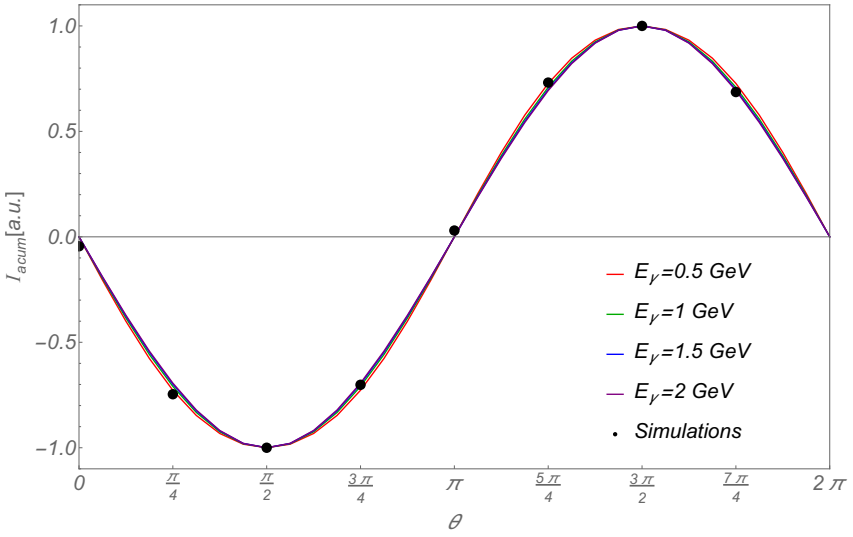

Figure 3.4: Comparison between the θ dependency of the produced current from theoretical predictions for various photon energies (colored lines) and the simulations (black dots).

- For $E_2 = 0$ there is no net current, and the drift of both species is suppressed since both electrons and positrons have transverse momentum distributions that peak at 0;
- The current increases until $E_2 \approx E_1$;
- For higher values of E_2, the peaks start getting closer together.

In order to see how E_2/E_1 affects the current in our case, I show a plot of $J2$ as a function of $x1$ at the end of the simulation for the various values of E_2/E_1 that were simulated. This plot is shown in figure 3.6, from which I can conclude that the maximum current production does in fact appear to be in a 1.5 ± 0.5

θ	N_{pairs}/N_γ	$\int J2dx1$ [10^{-3} pC/fsμm]
0	0.47	-0.3
$\pi/4$	0.47	-5.0
$\pi/2$	0.48	-6.7
$3\pi/4$	0.47	-4.8
π	0.47	0.2
$5\pi/4$	0.47	4.9
$3\pi/2$	0.47	6.7
$7\pi/4$	0.47	4.6

Table 3.2: Current density integral and ratio of the number of pairs with the initial number of photon for the simulated values of θ.

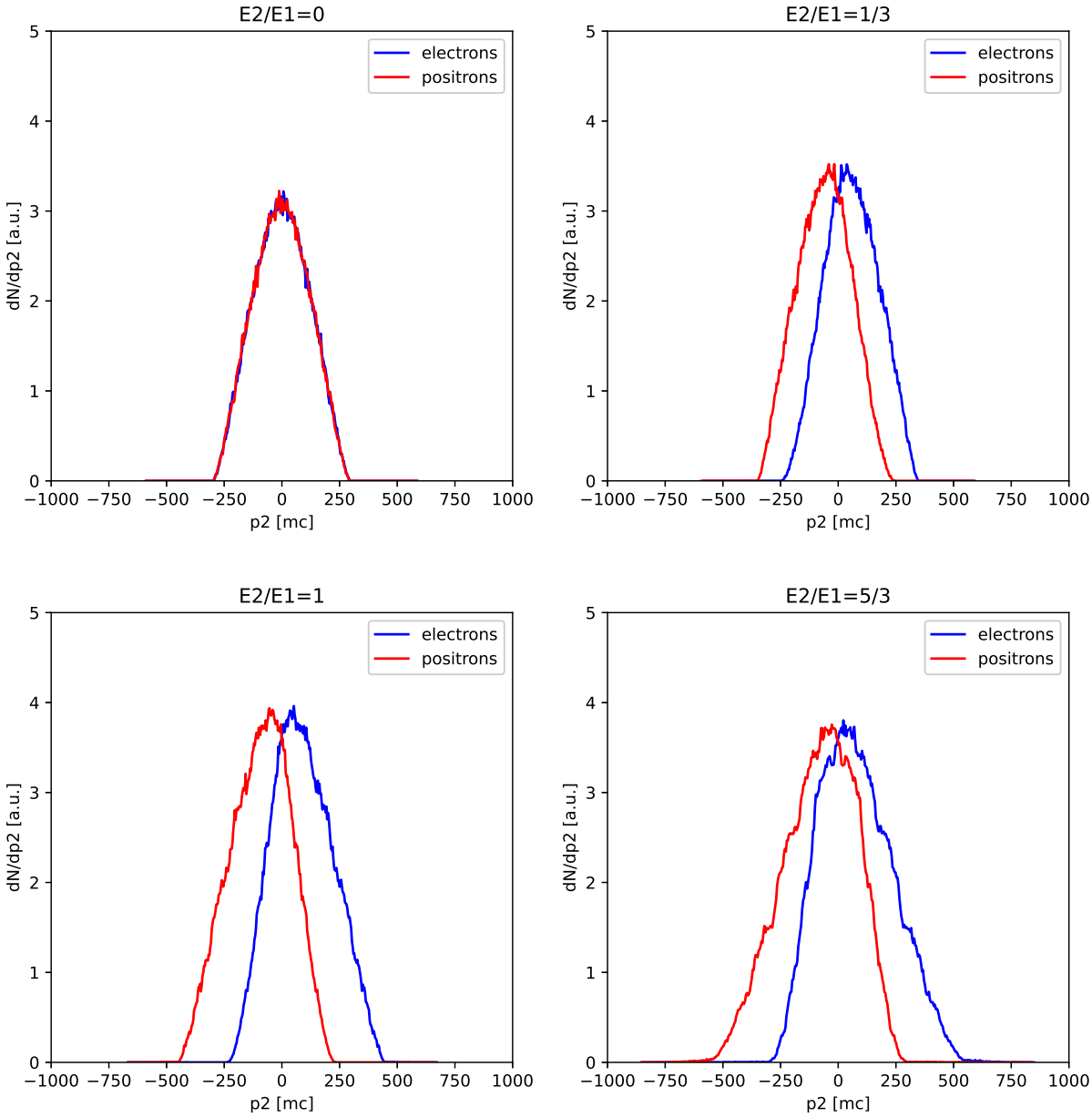

Figure 3.5: Plots of transverse momentum distribution dN/dp_2 for electrons (blue) and positrons (red) in various for values of E_2/E_1 of 0, 1/3, 1 and 5/3.

window. After the increase in peak current, the tendency is to once again decrease the charge separation and therefore the net current. However, unlike the θ variation, the case of increasing and decreasing E_2 without changing E_1 has a consequence on the number of pairs being produced. The ratio of pairs at the end of the simulation and photons at the start is shown in table 3.3. There is a correlation between the number of produced pairs and E_2/E_1, but despite this, the highest value for E_2/E_1 still doesn't maximize the current. Similarly to what was done for θ, the theoretical prediction and the simulation result can be compared. In figure 3.7 it can be seen that, although the agreement isn't as well achieved as in figure 3.4 for various values of photon energy, the behavior of both theory and simulation results are the same for energies close to $\hbar\omega_{crit}$ (which is 1.25 GeV for the photon spectrum used).

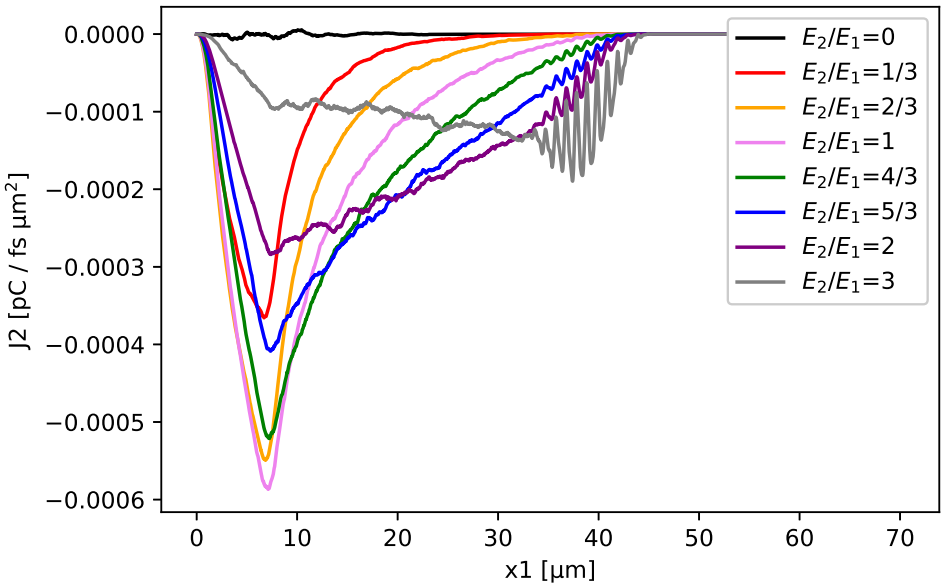

Figure 3.6: Current density $J2$ as a function of $x1$ at the end of the simulation for all the values of E_2/E_1 simulated. $J2$ was first averaged over $x2$ and then a moving average with a window of 100 points has been performed to remove noise from the output of the simulation.

E_2/E_1	N_{pairs}/N_γ	$\int J2dx1$ [10^{-3} pC/fsμm]
0	0.35	-0.01
1/3	0.38	-2.9
2/3	0.43	-5.1
1	0.47	-6.9
4/3	0.51	-7.4
5/3	0.55	-7.5
2	0.58	-6.9
3	0.64	-4.2

Table 3.3: Current density integral and ratio of the number of pairs with the initial number of photons for the simulated values of E_2/E_1.

It is important to note that despite the success of the theoretical model in predicting the behavior of the current, both in its direction and in the dependency of θ and E_2/E_1, these simulations are far from valid in a real laser-electron scattering experiment. Radiation reaction was completely neglected and the laboratory

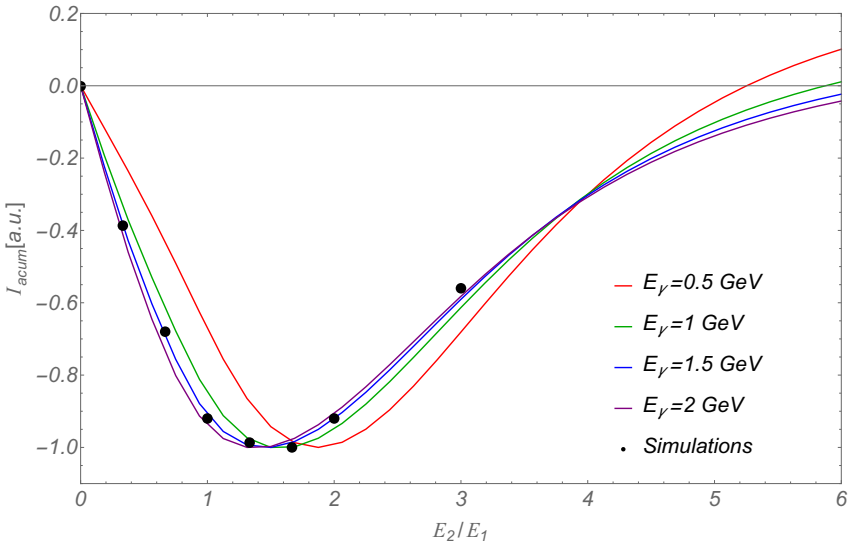

Figure 3.7: Comparison between the E_2/E_1 dependency of the produced current from theoretical predictions for various photon energies (colored lines) and the simulations (black dots).

lasers require a small spot size (in the order of tens of microns) to be able to achieve local intensities on the order of $10^{23} - 10^{24}$ W/cm^2. This means that in order to correctly predict what would happen in an actual experiment, I need to model a finite laser pulse and consider a fully quantum treatment of the interactions, with nonlinear Compton scattering and radiation reaction.

3.2 Phase Control and Charge Separation with a Finite Gaussian Laser Pulse, Including QED Radiation Reaction

I now input a finite spot size to both the laser pulse and generate the photons consistently from a relativistic electron beam in OSIRIS. For this study, I am using 2D PIC-QED simulations without periodicity in any direction. For the electron beam, I consider a mono-energetic beam with a gaussian density profile with the same standard deviation in all directions. The two-colored laser pulse is initialized by overlapping both laser frequencies using the same spot sizes. Since the pair production is linear with the number of electrons in the beam, one can extrapolate the total number of pairs or current generated for other electron beam charges. The laser focuses exactly when its center encounters the center of the electron beam. For this study, I ran 3 simulations for different values of θ, and for $E_2/E_1 = 1$, since this is a good value for current generation according to the previous section. The simulation parameters can be found in table 3.4.

Since the lasers in these simulations have a finite spot size, the separations of momentum that were shown in the previous section should give rise to a separation of charges in the $x2$ direction. In order to visualize this, I present in figure 3.8 the electron and positron distributions for $\theta = 0$ and $\theta = \pi/2$ after ≈ 98 fs from the beginning of the simulation time. In the case where $\theta = 0$, the electrons and positrons drift both in positive and negative $x2$ direction, so despite the drift of the particles, no charge separation is produced. However, for $\theta = \pi/2$ this is no longer true. Electrons have a preferential drift along the positive $x2$ direction

Variable	Value
ω_0	$\approx$ 1.9 x10^{15} Hz
a_1	300
E_2/E_1	1
θ	$\pi/2$, $\pi/4$, 0
$\tau_{rise} = \tau_{fall}$	$\approx$ 32 fs
Spot Size (both harmonics)	$\approx$ 12.8 μm
Number of cells	8640 x 1800
Box size	$\approx$ 70 x 80 μm
Δt	$\approx$ 2.6 as
Radiation Reaction	On
nonlinear Compton scattering	On
nonlinear Breit-Wheeler pair creation	On
Particles per cell	2 x 2
Electron beam peak charge density	$\approx$ 10 pC/μm^3
Electron beam energy γ	$\approx$ 5 GeV
Electron distribution standard deviation	$\approx$ 3.2 μm
Electron beam total charge	$\approx$ 32 pC

Table 3.4: Simulation parameters for the simulations with finite spot size. Only θ was varied.

while positrons show a preferential drift along the negative x2 direction. Due to radiation reaction, it is also observed that particles lose a large amount of their energy and begin co-propagating with the laser pulse (represented in purple).

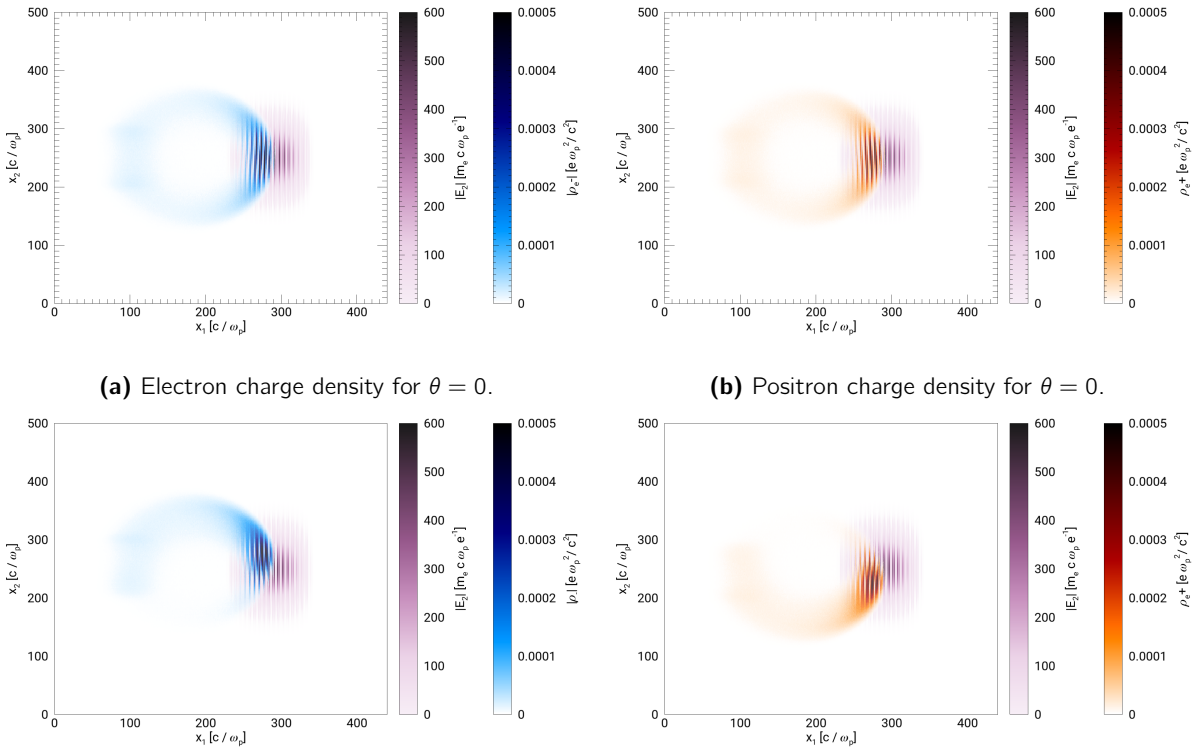

(a) Electron charge density for $\theta = 0$.

(b) Positron charge density for $\theta = 0$.

(c) Electron charge density for $\theta = \pi/2$.

(d) Positron charge density for $\theta = \pi/2$.

Figure 3.8: Charge density for electrons (in blue) and positrons (in red) for simulations with finite spot size with $\theta = 0$ (figures a) and b)) and $\theta = \pi/2$ (figures c) and d)).

The result of figure 3.8 achieves the main objective of this thesis: By controlling the phase offset θ between the two components of a two-colored laser pulse, it is possible to generate a current in the transverse direction and control the species separation among the generated electron-positron pairs. The fact that the laser eventually defocuses and liberates the particles that are co-moving with it ensures that given enough time (which is computationally non-viable to simulate in the present runs) the product of the scattering will be two beams, one consisting mostly of electrons and another one of positrons, moving at opposite angles with relation to the optical axis. For a better 3D visualization of the achieved separation, image 3.9 showcases how the two species are separated in space for the case of $\theta = 0$ and $\theta = \pi/2$. Here, it can be seen that for $\theta = 0$, the electrons and the positrons are overlapping in the laser beam and that the charges outside the laser influence have no preferential distribution. However, for $\theta = \pi/2$, the particles that already left the pulse are separated, and even the particles still oscillating inside the pulse are already physically separated.

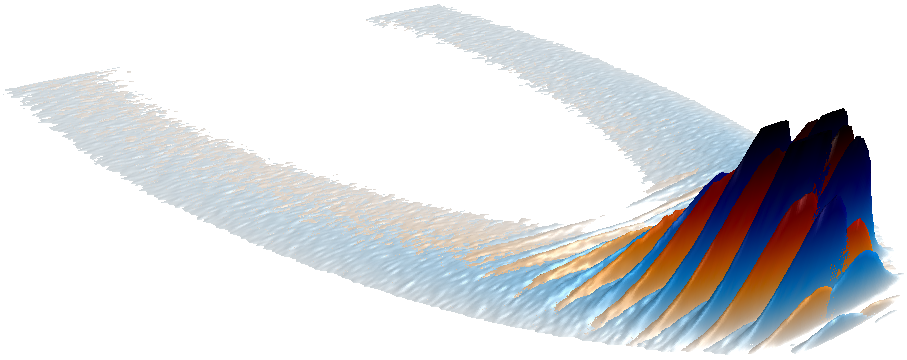

(a) Final charge density distribution with $\theta = 0$.

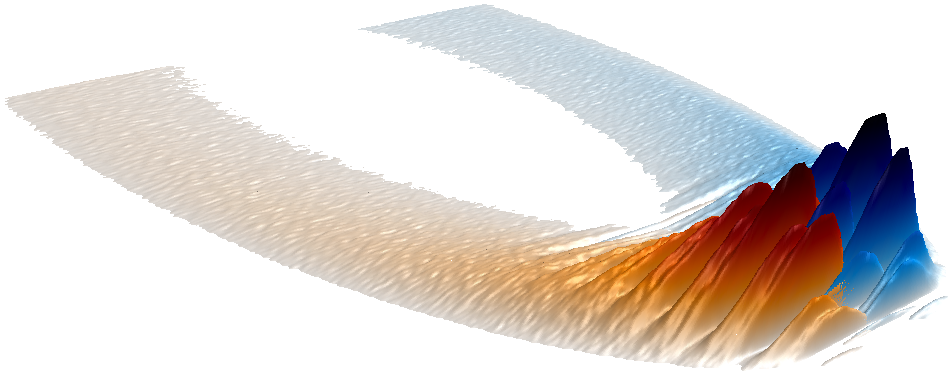

(b) Final charge density distribution with $\theta = \pi/2$.

Figure 3.9: 3D visualization of charge density of electrons (in blue) and positrons (in orange) of figures 3.8a, 3.8b, 3.8c and 3.8d. Regions with highly oscillatory behavior are still under the influence of the laser pulse, as the charged particles co-propagate with it.

Because both species get separated and move in opposite directions, $\theta = \pi/2$ is an ideal setup to maximize the produced current also in the finite-pulse scenario. A plot of the produced current both with $\theta = 0$ and $\theta = \pi/2$ is shown in figure 3.10. Here it is seen that the current deposited for $\theta = 0$ is barely

distinguishable from noise, except in the region where particles are still oscillating under the influence of the pulse (where the current is produced by that oscillation, and not an overall drift). Meanwhile, for $\theta = \pi/2$ there are two large concentrations of current, both in the same direction but on opposite sides of the optical axis, due to both species moving in opposite directions and having opposite charges. A study is performed to understand where the net current is more intense and how it changes for the simulated values of θ. I define $I2_T$ as being the total current in a slice of constant $x2$, i.e

$$I2_T = \int_{x1_{min}}^{x1_{max}} J2dx1 \ . \tag{3.2}$$

This allows for the visualization of how close the maximum current is to the optical axis while neglecting the current produced by the particles oscillating in the laser fields (since that contribution averages to 0 in the integral), therefore I present a plot for this total current in figure 3.11a. From this plot, it is visible that the maximum of the current occurs around 30 μm and 50 μm, and that $\theta = \pi/2$ has a higher peak current than $\theta = \pi/4$, which agrees with the results from the previous section. Since the spot size of the laser is around 12.8 μm and the optical axis is located at $x2 = 40$ μm, I can conclude that most of the particles that contribute to the net current are nearly outside the most intense laser region. It is also visible that this plot is not perfectly symmetrical around the optical axis and that there is a small current for the case of $\theta = 0$. This small current changes sign around the optical axis and corresponds to a contribution of the ponderomotive force that the electrons in the beam feel when crossing the pulse. If I subtract this contribution to the remaining plots, symmetry around the optical axis is now observed in the currents produced as seen in figure 3.11b.

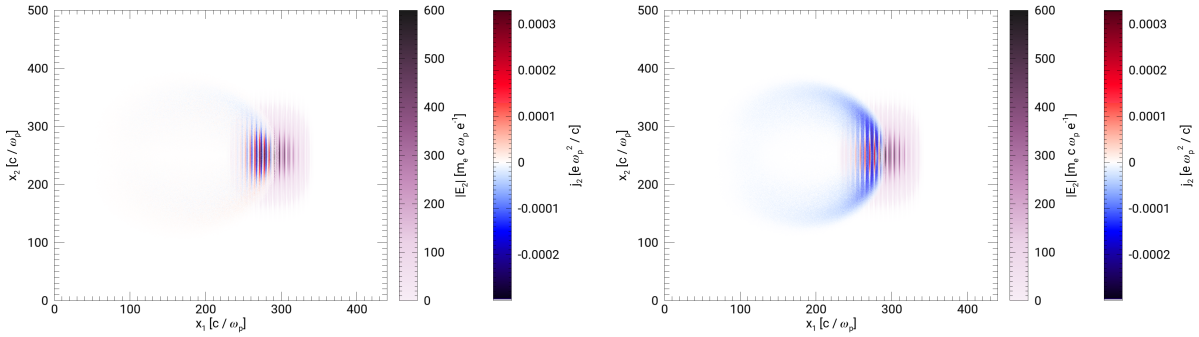

(a) Transverse current density for $\theta = 0$.

(b) Transverse current density for $\theta = \pi/2$.

Figure 3.10: Transverse electric current generated by the movement of the produced pairs for a) $\theta = 0$ and b) $\theta = \pi/2$.

Finally, I investigate the impact that θ has on the number of pairs present in the simulation. A table with the ratio of the number of created pairs and initial electrons in the beam is found in table 3.5. From here, it is visible that the variation of θ still keeps the variation in the number of pairs in the order of 2% as was concluded in the plane wave simulations, and therefore doesn't contribute significantly to the increase of current observed.

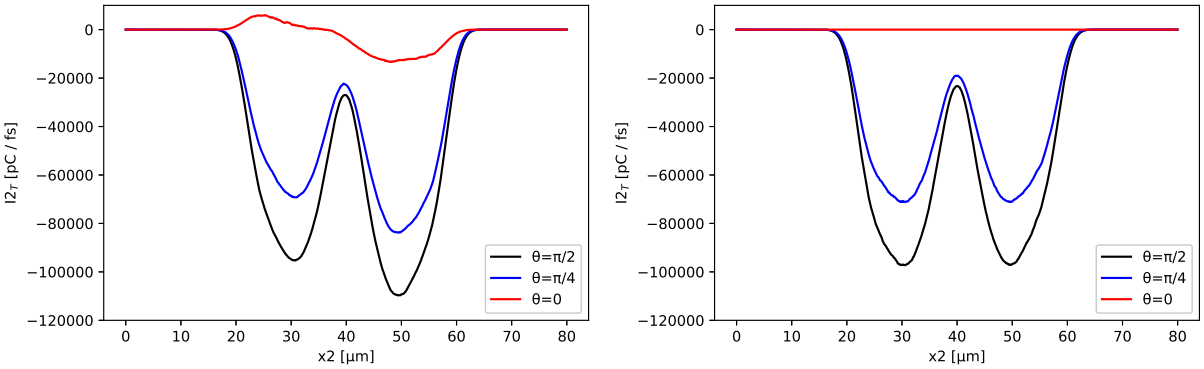

(a) Plot of $I2_T$ for $\theta = 0$, $\theta = \pi/4$ and $\theta = \pi/2$.

(b) Plot of $I2_T$ subtracting the contribution of $\theta = 0$.

Figure 3.11: Plots of $I2_T$ vs. $x2$ for $\theta = 0$, $\theta = \pi/4$ and $\theta = \pi/2$. A moving average with 20 points has been done to smooth the plot.

θ	N_{pairs}/N_{e^-}
0	6.0
$\pi/4$	6.1
$\pi/2$	6.1

Table 3.5: Ratio between number of pairs and initial number of electron for the values of θ simulated.

Chapter 4

Conclusions

This thesis deals with phase control of species separation in Breit-Wheeler electron-positron beams. The pairs are generated from a head-on collision of electrons with a two-colored laser pulse. The two-colored laser can be experimentally obtained by overlapping a laser beam with its second harmonic.

I have derived an analytical model for the separation of electron-positron pairs born amidst a two-colored laser pulse. The theoretical analysis reveals that spatial separation of electrons and positrons is directly related to the phase difference θ of the two laser modes, and by varying θ we can obtain a full separation or no separation at all. The phase scan can be used as a direct experimental signature of this effect.

The model assumes a transversely infinite plane wave for the laser beam. According to the analytical calculations, the optimal distribution of energy between the two harmonics is when the peak value of the electric field is comparable in each mode.

To confirm the validity of the theoretical description in non-ideal conditions, the same setup was studied with particle-in-cell simulations. The first verification was obtained using a plane wave with a finite envelope. This showed the same parametric dependencies as the model predicted. We then proceeded to full-scale, two-dimensional simulations, featuring a finite spot size, two-colored Gaussian laser pulse. Simulations of a head-on collision between a relativistic electron beam and this laser pulse were performed to further investigate the process of charge separation and show that the process could have macroscopic observable for laboratory experiments. We confirm that the maximum current generated by the particles being born via Breit-Wheeler pair creation in this setup occurs for phase differences of $\theta = \pm\pi/2$ and comparable values of the electric fields of each harmonic, just like the analytical estimates predict. This means that the effect is local, and the laser pulse transverse structure is not required to observe this process. For a single-mode laser (e.g. $E_1 = 0$ or $E_2 = 0$), the species separation is fully suppressed.

If the laser spot size is very small (of the order of the laser wavelength), it may happen that the ponderomotive force accelerates the charge separation once the leptons are first launched in opposite directions, and this could be a subject of a future investigation. Further work would include upgrading the theoretical model for it to predict the value of the obtained current density, instead of just identifying the optimal parameters where it is maximized. Computing the asymptotic angle of lepton escape in each direction would also be

of interest to guide the detector design for experiments. A detailed study of emitted radiation from this system could reveal an additional experimental signature, analogously to the THz radiation emitted by a similar setup of two-colored laser ionization.

Original Contributions

The work which has lead to the completion of this thesis has led to contributions in the following peer reviewed papers:

- B. Barbosa et al, to be submitted to MRE (2022) - Analytical description and simulation confirmation of phase control of of charge separation in Breit-Wheeler pairs using two-color pulses;

- B. Martinez, B. Barbosa, M. Vranic, submitted, ArXiv: https://arxiv.org/abs/2207.08728 - Calculations of low-energy pairs which are later used for plasma channel acceleration ;

- D. Ramsey et al, submitted (B. Barbosa in the Acknowledgments) - Enthusiastic discussions.

The work was presented at:

- PULSE Division Student Meeting, LLE, Rochester, June 2022;

- GoLP EPP Meeting, IST, November 2022.

Bibliography

[1] S. Weber *et al.*, "P3: An installation for high-energy density plasma physics and ultra-high intensity laser–matter interaction at eli-beamlines", *Matter and Radiation at Extremes*, vol. 2, no. 4, pp. 149–176, 2017.

[2] B. Cros and et al., *Laser plasma acceleration of electrons with multi-pw laser beams in the frame of cilex*, 2014.

[3] *Exawatt center for extreme light studies*.

[4] P. Goldreich and W. H. Julian, "Pulsar Electrodynamics", *Astrophysical Journal*, vol. 157, p. 869, Aug. 1969.

[5] M. A. Ruderman and P. G. Sutherland, "Theory of pulsars: polar gaps, sparks, and coherent microwave radiation." *Astrophysical Journal*, vol. 196, pp. 51–72, Feb. 1975.

[6] D. L. Burke *et al.*, "Positron production in multiphoton light-by-light scattering", *Phys. Rev. Lett.*, vol. 79, pp. 1626–1629, 9 Sep. 1997.

[7] M. Jirka, O. Klimo, M. Vranic, S. Weber, and G. Korn, "Qed cascade with 10 pw-class lasers", *Scientific Reports*, vol. 7, p. 15 302, Nov. 2017.

[8] H. Bethe and W. Heitler, "On the Stopping of Fast Particles and on the Creation of Positive Electrons", *Proceedings of the Royal Society of London Series A*, vol. 146, no. 856, pp. 83–112, Aug. 1934.

[9] B. Martinez, M. Lobet, R. Duclous, E. d'Humières, and L. Gremillet, "High-energy radiation and pair production by coulomb processes in particle-in-cell simulations", *Physics of Plasmas*, vol. 26, no. 10, p. 103 109, 2019.

[10] R. G. Greaves, M. D. Tinkle, and C. M. Surko, "Creation and uses of positron plasmas*", *Physics of Plasmas*, vol. 1, no. 5, pp. 1439–1446, 1994.

[11] N. P. Klepikov, "Emission of photons or electron-positron pairs in magnetic fields", *Zhur. Esptl. i Teoret. Fiz.*, vol. 26, 1954.

[12] G. Breit and J. A. Wheeler, "Collision of two light quanta", *Phys. Rev.*, vol. 46, pp. 1087–1091, 12 Dec. 1934.

[13] A. Galkin *et al.*, "Diagnostics of the peak laser intensity based on the measurement of energy spectra of electrons accelerated by the laser beam", *Proceedings of SPIE - The International Society for Optical Engineering*, vol. 7993, pp. 43–, Sep. 2010.

[14] M. Vranic, O. Klimo, G. Korn, and et al., "Multi-gev electron-positron beam generation from laser-electron scattering", *Sci Rep*, vol. 8, 2018.

[15] H. Hu, C. Müller, and C. H. Keitel, "Complete qed theory of multiphoton trident pair production in strong laser fields", *Phys. Rev. Lett.*, vol. 105, p. 080 401, 8 Aug. 2010.

[16] K. Kim, A. Taylor, J. Glownia, and G. Rodriguez, "Coherent control of terahertz supercontinuum generation in ultrafast laser–gas interactions", *Nature Photonics*, vol. 2, pp. 605–609, Jul. 2008.

[17] K. Qu, S. Meuren, and N. J. Fisch, "Signature of collective plasma effects in beam-driven qed cascades", *Phys. Rev. Lett.*, vol. 127, p. 095 001, 9 Aug. 2021.

[18] R. A. Fonseca *et al.*, "Osiris: A three-dimensional, fully relativistic particle in cell code for modeling plasma based accelerators", in *International Conference on Computational Science*, 2002.

[19] M. Vranic, T. Grismayer, J. L. Martins, R. A. Fonseca, and L. O. Silva, "Qed vs. classical radiation reaction in the transition regime", *AIP Conference Proceedings*, vol. 1777, no. 1, p. 050 006, 2016.

[20] M. Vranic, "Extreme laser-matter interactions: Multi-scale pic modelling from the classical to the qed perspective", Ph.D. dissertation, Instituto Superior Técnico, 2015.

[21] J. D. Jackson, *Classical Electrodynamics*, 3rd ed. Wiley, 1999.

[22] C. F. Nielsen *et al.*, "Experimental verification of the landau–lifshitz equation", *New Journal of Physics*, vol. 23, no. 8, p. 085 001, Aug. 2021.

[23] T. Nakamura, "On the schott term in the lorentz-abraham-dirac equation", *Quantum Beam Science*, vol. 4, no. 4, 2020.

[24] M. Tamburini, F. Pegoraro, A. D. Piazza, C. H. Keitel, and A. Macchi, "Radiation reaction effects on radiation pressure acceleration", *New Journal of Physics*, vol. 12, no. 12, p. 123 005, Dec. 2010.

[25] M. Vranic, J. Martins, R. Fonseca, and L. Silva, "Classical radiation reaction in particle-in-cell simulations", *Computer Physics Communications*, vol. 204, pp. 141–151, 2016.

[26] L. Landau and E. Lifshitz, *The Classical Theory of Fields. Course of Theoretical Physics*, 4th ed. Elsevier Science, 2013.

[27] W. H. Furry, "On bound states and scattering in positron theory", *Phys. Rev.*, vol. 81, pp. 115–124, 1 Jan. 1951.

[28] J. Schwinger, "On gauge invariance and vacuum polarization", *Phys. Rev.*, vol. 82, pp. 664–679, 5 Jun. 1951.

[29] C. Ridgers *et al.*, "Modelling gamma-ray photon emission and pair production in high-intensity laser–matter interactions", *Journal of Computational Physics*, vol. 260, pp. 273–285, 2014.

[30] J. M. Dawson, "Particle simulation of plasmas", *Rev. Mod. Phys.*, vol. 55, pp. 403–447, 2 Apr. 1983.

[31] B. Martinez, "Radiative and quantum electrodynamic effects in ultra-relativistic laser-matter interaction", Theses, Université de Bordeaux, Dec. 2018.

[32] J. P. Boris, "Relativistic plasma simulation-optimization of a hybrid code", *Proceeding of Fourth Conference on Numerical Simulations of Plasmas*, Nov. 1970.